

Special Section:

 ExoMars Trace Gas Orbiter -
One Martian Year of Science

This article is a companion to
Patel et al. (2021), <https://doi.org/10.1029/2021JE006837>.

Key Points:

- We provide the first detection of a high-altitude peak of ozone between 40 and 60 km in altitude over the north polar latitudes of Mars
- We confirm the presence of a previously detected, more prominent high-altitude ozone peak in the south polar latitudes
- Both high-altitude peaks are observed in the sunrise and sunset occultations, indicating that the layers could persist during the day

Correspondence to:

 A. S. J. Khayat,
alain.khayat@nasa.gov
Citation:

Khayat, A. S. J., Smith, M. D., Wolff, M., Daerden, F., Neary, L., Patel, M. R., et al. (2021). ExoMars TGO/NOMAD-UVIS vertical profiles of ozone: 2. The high-altitude layers of atmospheric ozone. *Journal of Geophysical Research: Planets*, 126, e2021JE006834. <https://doi.org/10.1029/2021JE006834>

Received 25 JAN 2021
Accepted 28 SEP 2021

© 2021 The Authors. This article has been contributed to by US Government employees and their work is in the public domain in the USA. This is an open access article under the terms of the [Creative Commons Attribution-NonCommercial-NoDerivs License](#), which permits use and distribution in any medium, provided the original work is properly cited, the use is non-commercial and no modifications or adaptations are made.



ExoMars TGO/NOMAD-UVIS Vertical Profiles of Ozone: 2. The High-Altitude Layers of Atmospheric Ozone

Alain S. J. Khayat^{1,2} , Michael D. Smith¹ , Michael Wolff³ , Frank Daerden⁴ ,
Lori Neary⁴ , Manish R. Patel⁵ , Arianna Piccialli⁴ , Ann C. Vandaele⁴,
Ian Thomas⁴ , Bojan Ristic⁴ , Jon Mason⁵, Yannick Willame⁴, Cedric Depiesse⁴,
Giancarlo Bellucci⁶, and José Juan López-Moreno⁷

¹Planetary Systems Laboratory, Solar System Exploration Division, NASA Goddard Space Flight Center, Greenbelt, MD, USA, ²Department of Astronomy, Center for Research and Exploration in Space Science & Technology (CRESST II), University of Maryland, College Park, MD, USA, ³Space Science Institute, Boulder, CO, USA, ⁴Royal Belgian Institute for Space Aeronomy BIRA-IASB, Brussels, Belgium, ⁵School of Physical Sciences, The Open University, Milton Keynes, UK, ⁶Instituto di Astrofisica e Planetologia Spaziali, IAPS-INAF, Rome, Italy, ⁷Instituto de Astrofisica de Andalucia, IAA-CSIC, Glorieta de la Astronomia, Granada, Spain

Abstract Solar occultations performed by the Nadir and Occultation for Mars Discovery (NOMAD) ultraviolet and visible spectrometer (UVIS) onboard the ExoMars Trace Gas Orbiter (TGO) have provided a comprehensive mapping of atmospheric ozone density. The observations here extend over a full Mars year (MY) between April 21, 2018 at the beginning of the TGO science operations during late northern summer on Mars (MY 34, $L_s = 163^\circ$) and March 9, 2020 (MY 35). UVIS provided transmittance spectra of the Martian atmosphere allowing measurements of the vertical distribution of ozone density using its Hartley absorption band (200–300 nm). The overall comparison to water vapor is found in the companion paper to this work (Patel et al., 2021, <https://doi.org/10.1029/2021JE006837>). Our findings indicate the presence of (a) a high-altitude peak of ozone between 40 and 60 km in altitude over the north polar latitudes for at least 45% of the Martian year during midnorthern spring, late northern summer-early southern spring, and late southern summer, and (b) a second, but more prominent, high-altitude ozone peak in the south polar latitudes, lasting for at least 60% of the year including the southern autumn and winter seasons. When present, both high-altitude peaks are observed in the sunrise and sunset occultations, suggesting that the layers could persist during the day. Results from the Mars general circulation models predict the general behavior of these peaks of ozone and are used in an attempt to further our understanding of the chemical processes controlling high-altitude ozone on Mars.

Plain Language Summary The presence of ozone in the Martian atmosphere has been observed since it was first detected by the 1969 and 1971 Mariner flyby missions. Mars is known to have a permanent ozone layer below 30 km. Solar occultations performed by the ultraviolet and visible spectrometer onboard the ExoMars Trace Gas Orbiter have provided a comprehensive mapping of the vertical distribution of ozone in the atmosphere of Mars for an entire Mars year, describing the seasonal, spatial, and local time distribution of ozone in detail. This analysis indicates the presence of a previously undetected high-altitude peak of ozone between 40 and 60 km in altitude over the north polar latitudes for approximately half of the Martian year. It also confirms the presence of a second, but more prominent, high-altitude ozone peak in the south polar latitudes. When they are present, both high-altitude peaks are observed in the sunrise and sunset occultations, indicating that the layers could persist during the day.

1. Introduction

The presence of ozone (O_3) in the Martian atmosphere has been observed since it was first detected by the ultraviolet spectrometer experiments on the 1969 and 1971 Mariner flyby missions (Barth & Hord, 1971; Barth et al., 1972, 1973). Ozone is sensitive to changes in the incoming solar ultraviolet (UV) flux on the planet. It is mainly formed by the three-body reaction involving molecular (O_2) and atomic oxygen (O) that are byproducts of the photolysis of CO_2 , the main atmospheric constituent on Mars (molar fraction $\sim 95\%$). In the opposite direction, ultraviolet radiation during the day destroys O_3 back to O, O_2 , and $O_2(^1\Delta_g)$. The abundance of ozone is regulated locally by the presence of the odd hydrogen species (H, OH, and HO_2)

produced by the photolysis of water vapor (H_2O). The odd hydrogen species play a major role in regenerating the photo-dissociated CO_2 in the upper atmosphere, therefore helping to stabilize the Martian atmosphere (e.g., Lefèvre et al., 2004; Perrier et al., 2006).

The periodic monitoring of O_3 on Mars includes observations from the ground and from space using flyby missions, Mars orbiting satellites, and space telescopes. Due to the presence of telluric O_3 that renders the terrestrial atmosphere opaque, ground-based observations have used heterodyne infrared spectroscopy to measure total column abundances of O_3 from its Doppler-shifted absorption lines around $9.7 \mu\text{m}$ (Espenak et al., 1991; Fast et al., 2006). The observations provided a confirmation of the odd hydrogen activity that predicts anticorrelation of ozone and water vapor abundances (e.g., Clancy & Nair, 1996; Clancy et al., 2016). Indirect observations of O_3 from the Earth (Novak et al., 2002; Noxon et al., 1976) targeted the $\text{O}_2(^1\Delta_g)$ produced by the photolysis of ozone, as it is characterized by an emission band system around $1.27 \mu\text{m}$ tracing the presence and abundance of ozone in the middle atmosphere ($\sim 25 \text{ km}$).

Space-based observations of Mars include UV observations of the Hartley band (200–300 nm) of ozone by the Faint Object Spectrograph onboard the Hubble Space Telescope at $L_s = 63.5^\circ$ during Mars' late northern spring (Clancy et al., 1996). The measurements show low-latitude O_3 abundances that are significantly elevated ($>100\%$) compared to the ones taken during northern fall ($L_s = 208^\circ$) by Espenak et al. (1991). This large increase is consistent with photochemical models due to large annual variations in the photochemistry on Mars (Clancy & Nair, 1996).

Measurements of the global distribution of ozone column abundance were made using continuous UV observations of Mars by the Mars Reconnaissance Orbiter (Clancy et al., 2016) and Mars Express (Perrier et al., 2006). The Mars Color Imager (MARCI) on MRO included a pair of UV imaging channels centered within (260 nm) and outside (320 nm) the O_3 Hartley band (Malin et al., 2001, 2008). This imaging system allowed daytime (local time of 3 p.m.) measurements of the total column abundance of O_3 using its absorption against the solar UV radiation reflected from the surface of Mars and atmospheric scattering. The observations by Clancy et al. (2016) provided daily global mapping of ozone from mid Mars Year (MY) 28 (November 2006, $L_s \sim 130^\circ$) when MARCI began its observations to the end of MY 32 (June 2015, $L_s \sim 360^\circ$). The results show elevated abundances at high northern and southern latitudes over the fall-winter-spring seasons, as well as at low latitudes around Mars aphelion ($L_s = 30^\circ$ – 120°).

Dayside observations with UV spectroscopy by the Spectroscopy for the Investigation of the Characteristics of the Atmosphere of Mars (SPICAM) instrument onboard Mars Express also provided distribution of the total column concentration of O_3 from nadir spectra in the 110–320-nm range (Perrier et al., 2006). The reported observations extended between January 2004 and April 2006, covering a full Mars year between $L_s = 331^\circ$ of MY 26 and $L_s = 37^\circ$ of MY 28. When compared to a general circulation model (e.g., Lefèvre et al., 2004), the behavior of ozone is in good overall agreement showing high variability at the northern high latitudes around late winter-early spring, and an increase in O_3 around the equator during the aphelion season. However, the general circulation model predictions underestimated the column abundance of O_3 at high latitudes in both hemispheres during northern spring (southern autumn) when compared to the retrieved SPICAM values. Willame et al. (2017) tracked the seasonal evolution of the ozone column using SPICAM data between late MY 26 and the end of MY 30. Large ozone abundances were observed over the winter poles with the condensation of atmospheric water, also seen by previous observations including those by SPICAM (Perrier et al., 2006) and MARCI (Clancy et al., 2016).

The vertical distribution of ozone in the atmosphere is very diagnostic in delineating the role that photochemistry plays at the different levels in the atmosphere at various seasons. The earliest attempts to provide vertical profiles from solar occultations yielded the first detection of O_3 in the middle atmosphere of Mars using the *Phobos 2* spacecraft, with values nearing 10^8 molecules/ cm^3 (Blamont & Chassefière, 1993). On the other hand, stellar occultations to retrieve vertical profiles and probe the evolution of ozone during nighttime on Mars were performed by SPICAM (Lebonnois et al., 2006). The observations covered latitudes between 30°S and 60°N during early northern spring ($L_s = 8^\circ$ – 50°) and autumn ($L_s = 155^\circ$ – 270°), and the southern hemisphere during southern autumn and winter ($L_s = 20^\circ$ and 155°).

These nighttime observations from stellar occultations were limited in frequency and coverage but provided initial clues to the presence of a near-surface ozone layer below 30 km and a nocturnal layer in the altitude

range 20–50 km, later confirmed by Lefèvre et al. (2007). The presence of ozone near the surface is expected due to solar UV radiation screening by CO₂ which limits the solar UV radiation that photolyzes O₃ and inhibits the presence of the hydroxyl radicals (HO_x) produced by H₂O photolysis (e.g., Daerden et al., 2019). The ozone enhancement peaks in the dry polar winter regions where atmospheric water vapor is suppressed near the ground (e.g., Daerden et al., 2019; Lefèvre et al., 2004). The ozone layer between 20 and 50 km is expected to form at night after the removal of O₃ by the solar UV radiation during the day, and then its regeneration after sunset (Lebonnois et al., 2006). The results from SPICAM show an increase in the O₃ abundance in the nocturnal layer before $L_s = 40^\circ$ around mid and low latitudes, reaching peak abundances $6\text{--}9 \times 10^9$ molecules/cm³ around altitude 40 km, before dissipating by $L_s = 130^\circ$. However, these stellar occultations were limited to nighttime, and the solar occultation observations presented here are needed to track the evolution of this layer.

Partly based on the SPICAM experience, Gröller et al. (2018) detected O₃ in 70 stellar occultations that were executed with the Imaging UltraViolet Spectrograph (IUVS) instrument of the Mars Atmosphere and Volatile EvolutioN (MAVEN) mission. The provided O₃ profiles were generally confined between ~20 and 60 km. Similarly to Lebonnois et al. (2006), but with a factor of 5 lower abundance, a nocturnal peak in ozone density is seen around an altitude of 40 km in the five ozone profiles retrieved during late northern spring ($L_s = 63^\circ$) over latitude 28°N, with abundances at the peak reaching a maximum $\sim 2 \times 10^9$ molecules/cm³. The occultations analyzed by Gröller et al. (2018) were also taken during nighttime, and were sparse in time and geography as they presented snapshots in time around $L_s = 21^\circ, 63^\circ, \text{ and } 124^\circ$.

Olsen et al. (2020) reported the first observations of ozone absorption between 3.279 μm (3,050 cm⁻¹) and 3.317 μm (3,015 cm⁻¹) in the infrared, using the midinfrared channel of the Atmospheric Chemistry Suite (ACS) “MidInfraRed” (MIR) onboard TGO. The retrievals from 15 observations provided O₃ profiles below 30 km at high northern latitudes (>65°N) around the northern fall equinox ($L_s = 160^\circ\text{--}190^\circ$). These profiles indicate a gradual transition of ozone toward the surface by showing an increase in the ozone density at lower latitudes, reaching 10¹⁰ molecules/cm³ below 10 km in agreement with Lebonnois et al. (2006) and Montmessin and Lefèvre (2013).

Three-dimensional photochemistry models have been used to investigate the behavior of the vertical distribution of ozone (Daerden et al., 2019; Montmessin & Lefèvre, 2013). In particular, Montmessin and Lefèvre (2013) discussed the ozone enhancement seen by earlier analyses of the SPICAM data (Lebonnois et al., 2006) that appeared at 50 km in the southern hemisphere above the winter pole, with no apparent counterpart over the north pole. They showed that the O₃ formation process is more efficient in the south where oxygen-rich air is largely transported from sunlit regions all the way to the polar regions, leading to the formation of ozone at night when oxygen atoms recombine.

However, Daerden et al. (2019) have presented a more complete picture of the vertical distribution of O₃ on Mars using the Global Environmental Multiscale (GEM) Mars general circulation model (GEM-Mars), which predicts the formation of a layer of O₃ at 40–60 km in altitude between 60° and 90°N, lasting between $L_s = 170^\circ$ and $L_s = 30^\circ$ of the following year, with minimum abundances in O₃ reached at $L_s = 270^\circ$.

The existence of ozone data sets that encompass the full seasonal cycle, as well as more complete latitudinal and vertical coverage, would be extremely valuable for understanding photochemistry in the Martian atmosphere and for further improving the existing photochemical models. In this work, we take advantage of the ExoMars Trace Gas Orbiter NOMAD/UVIS solar occultation observations for a full Mars year to focus on characterization of the high-altitude peak of ozone, tracking its latitudinal, vertical, local time (LT), and seasonal dependencies. This work is undertaken in parallel to a companion study of the climatology of ozone and its abundance with respect to water vapor, performed using the same data set from the NOMAD/UVIS instrument (Patel, 2021).

In Section 2, we describe the NOMAD instrument, the solar occultation observations used in this work, and we present the transmittance spectra at various altitudes in the Martian atmosphere showing the Hartley band absorption of ozone. In Section 3, we provide information on the retrieval process that derives vertical density profiles of O₃ from line-of-sight opacities through the atmosphere. In Section 4, we describe the GEM-Mars model. The retrieval results tracking the presence of the high-altitude peak of ozone and their

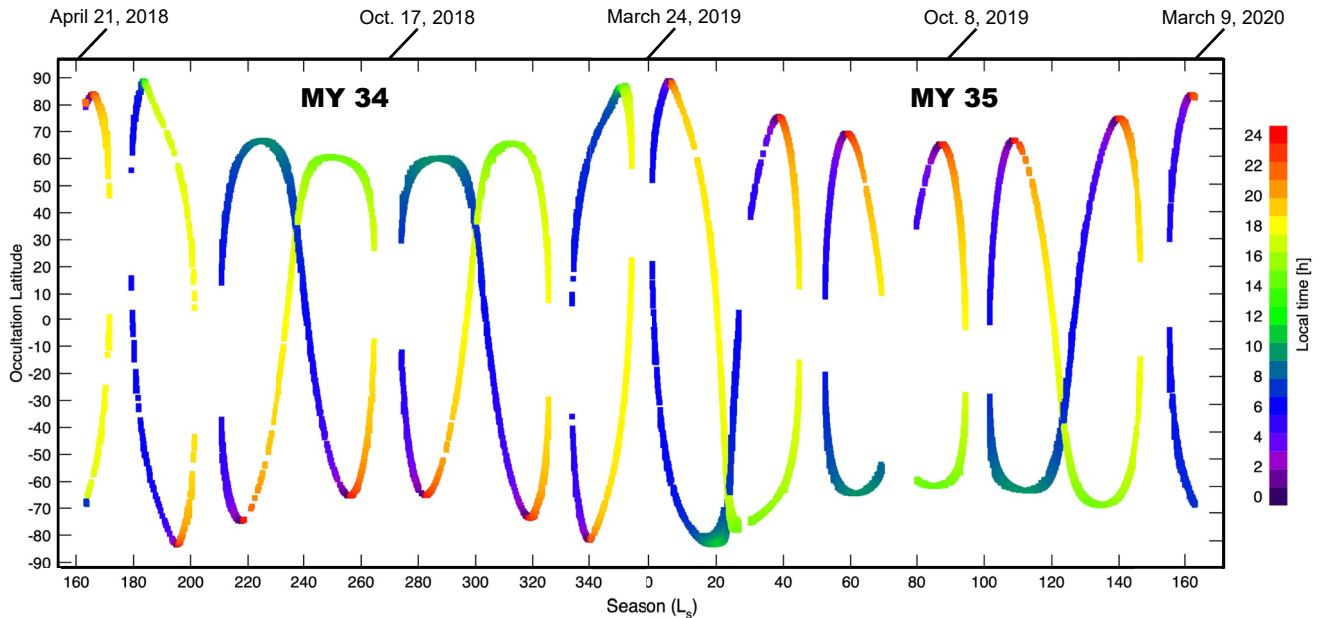


Figure 1. The seasonal (L_s), latitudinal, and local time distribution of the ultraviolet and visible spectrometer (UVIS) observations used in this work. The $L_s = 163^\circ$ at the start of the plot corresponds to the beginning of the observations on April 21, 2018, in MY 34. The gaps in the observations are mostly due to the atmosphere not always occulting the line-of-sight. Most of the local times covered during the occultations are before LT 10:00 h and after 18:00 h. We made use of observations to retrieve the vertical distribution of atmospheric ozone on Mars for a full Martian year at a vertical resolution <1 km.

comparison with GEM-Mars model outputs are presented in Section 5, and we finally discuss and summarize the findings of this work in Section 6.

2. Data Set: Spacecraft, Instrument, and Observations

2.1. NOMAD Instrument

The ExoMars Trace Gas Orbiter (TGO) has been returning data from Mars since April 21, 2018 ($L_s = 163^\circ$). The spacecraft is in a near-circular orbit with an inclination of 74° , orbiting Mars every ~ 2 hr at an average distance of 400 km from the surface of the planet with a precessing orbit that covers different local times (Vandaele et al., 2018). The Nadir and Occultation for Mars Discovery (NOMAD) is a spectrometer suite onboard TGO, providing observations in the nadir, limb, and solar occultation (SO) modes.

The wavelength coverage of NOMAD is in the near-infrared range with the SO spectrometer (2.3–4.3 μm) and the Limb Nadir Solar Occultation (LNO, 2.3–3.8 μm). It also covers portions of the ultraviolet-visible range with the ultraviolet and visible spectrometer UVIS between 200 and 650 nm (Patel et al., 2017).

UVIS is a single spectrometer unit within NOMAD that is capable of receiving light from two separate telescopes, one for the nadir mode and another for the solar occultation mode where the incoming light is directed using a periscope (Patel et al., 2017). This dual-telescope setup then feeds light via a selection mechanism into a single spectrometer that provides a spectral resolution of $\Delta\lambda = 1.2$ – 1.6 nm in the registered spectrum on a detector array of $1,024 \times 256$ pixels. The field of view (FOV) of UVIS is a circular aperture covering 2 arcmin in the sky. A more detailed description of the design and performance of UVIS can be found in Vandaele et al. (2015) and Patel et al. (2017).

2.2. UVIS Solar Occultation Observations

The solar occultation observations covered in this study extend over a full Mars year (687 Earth days) from MY 34 at $L_s = 163^\circ$ to MY 35 at the same L_s , corresponding to April 21, 2018 and March 9, 2020, respectively. The seasonal coverage for the full Mars year at the different latitudes and local times is shown in Figure 1.

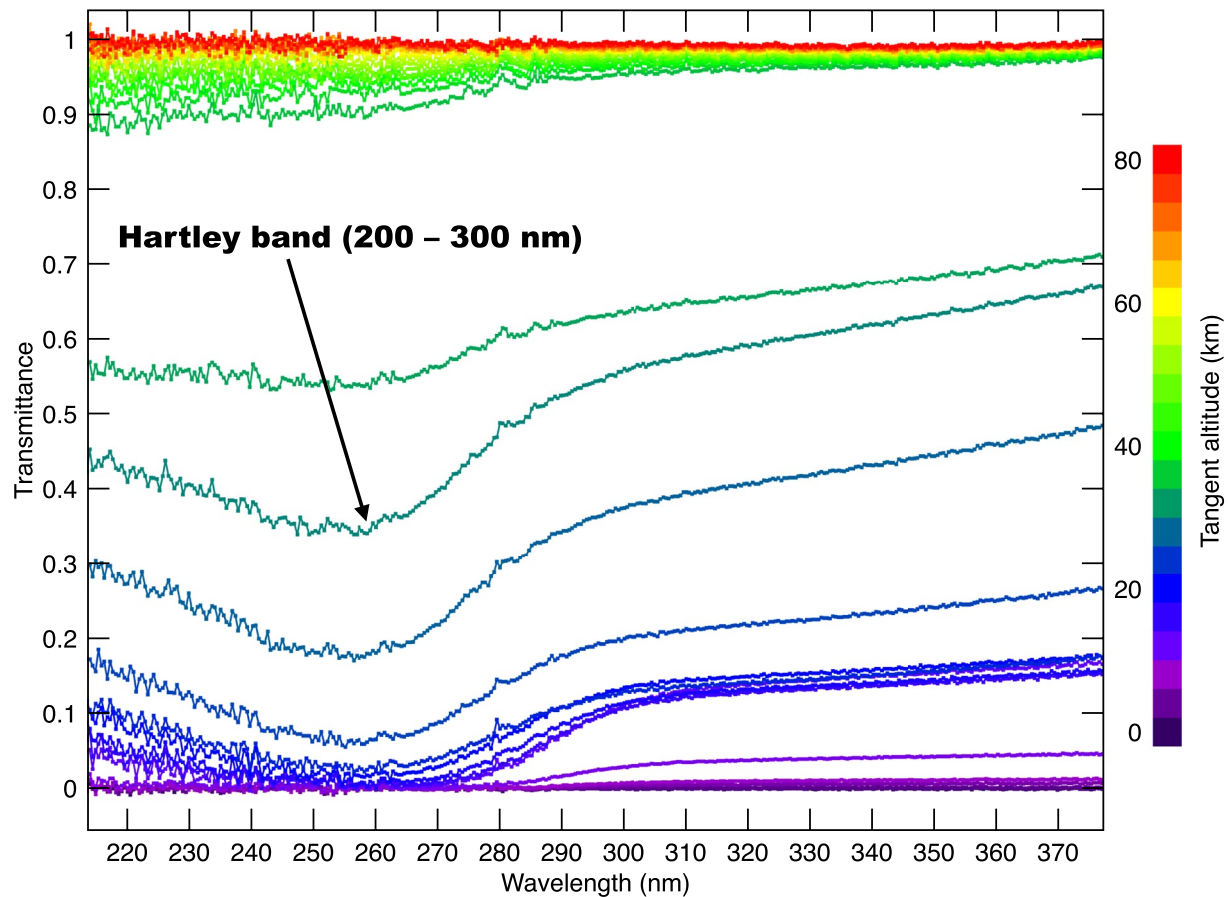


Figure 2. Example of typical ultraviolet and visible spectrometer (UVIS) atmospheric transmittance spectra from a solar occultation observation (nmd_cal_sc_uvvis_20180503t012553-20180503t014247-e) taken at egress on May 3, 2018 around the beginning of the Trace Gas Orbiter (TGO) science phase at $L_s = 169^\circ$ at mean occultation latitude 74.9°N and mean longitude -87.1°E , spanning LT = 19.0 and 19.3 h. As indicated by the color bar, high transmittance spectra belong to the upper parts of the atmosphere whereas low transmittance spectra belong to the lower parts close to the surface of Mars. The prominent absorption that is centered around 250 nm belongs to the ozone Hartley band, used to retrieve the abundance of O_3 .

The observations begin at $L_s = 163^\circ$ and extend to $L_s = 360^\circ$ at the end of MY 34, and continue to $L_s = 163^\circ$ of the following MY 35.

The atmosphere is typically sampled up to twice during each orbit at the ingress and egress configurations from the surface up to 200 km in altitude. However, the orbital inclination of TGO does not allow solar occultations to be continuously performed when the beta angle between the orbital plane of the spacecraft and the vector pointing toward the sun exceeds 67° (Vandaele et al., 2018). Therefore, this angle defines the frequency of the observations by UVIS (see Figure 1). In this study, 20% of the observations cover the equatorial latitudes $\pm 30^\circ$, 45% cover the midlatitudes 30° – 60°N and 30° – 60°S , and 35% cover latitudes poleward of 60°N and 60°S .

As the spacecraft passes behind the planet during an ingress and reemerges during egress, the solar radiance is attenuated by the atmosphere along the instrument's line-of-sight, therefore providing information on the atmospheric composition at different altitudes.

2.3. UVIS Solar Occultation Spectra

The solar occultations cover latitudes between 89°N and 84°S , with $\sim 4,100$ observations in total, averaging 35 spectra per occultation, where one spectrum is taken at a tangent altitude. Figure 2 represents typical solar occultation spectra at different tangent altitudes, spanning the range from the surface of Mars to the

top of the atmosphere (i.e., where the transmittance is unity). These data are taken from the region of UVIS wavelength range used for the work we present here, that is, between 220 and 370 nm.

Each transmittance spectrum is obtained by dividing the solar radiation through the Martian atmosphere as received at UVIS by the solar irradiance at UVIS of a reference spectrum outside the atmosphere. The transmittance spectra in the observation were taken around late northern spring above northern latitudes. The spectra clearly show the presence of the Hartley absorption band of O₃ at 250 nm (220–300 nm), and the overall continuum level set by the absorption of suspended dust aerosols in the Martian atmosphere. As a result, the atmospheric opacity increasingly attenuates the signal at the lowest altitudes before the signal is completely lost close to the surface. The signal-to-noise ratio (SNR) in the spectra follows the transmittance. In the continuum around 300–330 nm outside the O₃ band, the measured SNR varies between ~750 at 65 km down to ~140 at 20 km. We made use of such observations to provide the seasonal distribution of the vertical abundance of atmospheric O₃ across Mars.

3. Ozone Retrieval Process

The retrieval process of the vertical distribution of ozone is discussed in detail in the companion paper (Patel et al., 2021) and is only briefly summarized here. The transmittance spectra (Figure 2) along the line-of-sight (LoS) at the respective tangent altitudes are converted during a two-step process into ozone number densities (n_{O_3} , molecules/cm³).

The first step begins with fitting the wavelength dependent transmittance along the LoS using the nonlinear least square fitting algorithm, the Levenberg-Marquardt (Markwardt, 2009), by minimizing the residuals between the observed spectrum and the computed one. Outside the ozone absorption band, the linear part of the transmittance spectra over the narrow range between 320 and 360 nm accounts for the contribution from the aerosol opacity and is used for the aerosol abundance determination. The contribution from Rayleigh scattering is characterized in the region between 220 and 230 nm across the ozone band (Ityaksov et al., 2008). An iterative process involving the aerosol abundance, Rayleigh scattering, and the Angstrom coefficient is performed until convergence. The column abundance of ozone along the occultation LoS is then retrieved by fitting the 240–320 nm portion of the Hartley band with the retrieved aerosol abundance values and the updated scattering contribution. The channels below 240 nm are characterized by a loss in responsivity of the detector at these wavelengths (Patel et al., 2017) and are therefore excluded from the fitting process.

The second step of the retrieval process is the inversion of the retrieved LoS abundance of ozone into a vertical profile for the number density (n_{O_3}) at the midpoint between two atmospheric layers, using the standard onion peeling method (Auvinen et al., 2002; Quémerais et al., 2006; Rodgers, 2000) and assuming a spherically symmetric atmosphere. Examples of a retrieved ozone vertical profile obtained through this method are shown in Figure 5 of Patel (2021).

4. GEM-Mars Model Description

The expected behavior of ozone in the Martian atmosphere can be simulated in general circulation models with additional routines for photochemical calculations (Daerden et al., 2019; Lefèvre et al., 2004). For the comparison of our O₃ retrievals, we use the GEM-Mars GCM (Daerden et al., 2019; Neary & Daerden, 2018).

GEM-Mars is operated on a grid with a horizontal resolution of 4° × 4° and with 103 vertical levels reaching from the surface to ~150 km. It calculates atmospheric heating and cooling rates by solar and infrared radiation through atmospheric CO₂, dust and ice particles, and solves the primitive equations of atmospheric dynamics, using a time step of 30 s. The model simulates the evolution of dust, water vapor and water ice, CO₂ and CO₂ ice, and tracers for chemical composition. The chemistry routines in GEM-Mars calculate the photochemistry and gas-phase interactions of CO₂, H₂O, and their photochemical products, including O₃ (Daerden et al., 2019). Comparisons of total ozone columns to observations of MARCI were presented in Daerden et al. (2019) and showed a good correspondence throughout most of the Martian year and across most latitudes. Deviations from the MARCI observations were attributed to imperfections in the simulation of the water cycle. GEM-Mars currently uses bulk condensation of water vapor onto monodisperse

ice particles of prescribed radius. While this simple treatment results in a reasonable simulation of the water cycle when compared to for example, Mars Reconnaissance Orbiter (MRO) Compact Reconnaissance and Imaging Spectrometer for Mars (CRISM) observations (Daerden et al., 2019; Smith et al., 2018), it may explain the deviations that still exist, although models with more sophisticated schemes show more or less similar biases (e.g., Navarro et al., 2014; Shaposhnikov et al., 2018).

The NOMAD-UVIS O₃ solar occultation data set now allows for a first detailed evaluation of the simulated vertical distribution of O₃ in the model. In this paper, we use a GEM-Mars simulation for generic conditions as presented in Daerden et al. (2019), with a self-consistently calculated dust distribution for an average nonglobal dust storm year. This has to be taken into account in the comparisons, as during the first year of NOMAD's science operations, a global dust storm occurred.

5. Results and Discussion

5.1. Vertical O₃ Profiles Over Polar Latitudes

The most recognizable trend pertaining to the seasonal distribution of ozone is that the highest abundances are observed over the winter poles (e.g., Barth & Hord, 1971; Clancy et al., 2016; Perrier et al., 2006; Willame et al., 2017). Figure 3 shows ~850 ozone vertical profiles as retrieved from ~24,300 spectra at selected seasonal bins over the north polar latitudes (60°–88.7°N). The seasonal bins are selected based on the frequency of the NOMAD coverage and to combine similarly behaving profiles in each bin. This provides a clear understanding of the seasonal evolution of the vertical profiles. The main “surface” layer of ozone on Mars is confined below 30 km, but as stated in Section 1, our focus throughout this study is the characterization and evolution of high-altitude peaks of ozone that form above 30 km.

In Figure 3a ($L_s = 0^\circ\text{--}25^\circ$), we detect a high-altitude peak of ozone that is clearly visible in the altitude range 42–63 km, reaching its maximum intensity around 50 km, with abundance values ranging between $n_{\text{O}_3} = 2 \times 10^7$ and 1×10^8 molecules/cm³. As time progresses, the peak persists in its shape and altitude throughout early northern spring in the $L_s = 0^\circ\text{--}25^\circ$ range. After $L_s = 25^\circ$, we notice changes in the shape of the vertical profile where ozone densities around 40 km have increased, weakening the inflection in the profile that existed at that altitude, filling the minimum in ozone between the high-altitude peak of ozone and the surface layer. The high-altitude peak maintains high concentrations of ozone, but the average enhancement ($\times 2$) of ozone density at around 35 km lowers the contrast between the ozone abundances at 35 and 50 km. Between $L_s = 45^\circ$ and 120° , the latitude range observed by UVIS is limited to 60°–70°N, indicating the absence of the high-altitude peak, and an ozone density gradually decreasing with height from 30 to 70 km. In midnorthern summer where polar latitudes are sampled, a high-altitude but weaker peak reappears around 55 km, with ozone densities in the $8 \times 10^6\text{--}4 \times 10^7$ molecules/cm³ range, and this persists between $L_s = 120^\circ$ and 210° . The overall behavior of ozone is well maintained above 50 km until $L_s = 210^\circ$. During early northern fall to midnorthern winter ($L_s = 210^\circ\text{--}330^\circ$), the latitudinal coverage is again reduced to latitudes below 70°N. There is no major presence of a high-altitude peak, with lower values of ozone throughout the entire vertical range. The high-altitude peak reemerges at the end of northern winter ($L_s = 330^\circ\text{--}360^\circ$), with increasing densities at the peak between 8×10^6 and 10^8 molecules/cm³ at around 45 km in altitude. It persists for at least 45% of the Martian year.

The ~910 vertical profiles derived from ~31,600 spectra taken over the south polar latitudes (60°–83.4°S) are shown in Figure 4. A high-altitude ozone peak appears in panel a at 45 km between $L_s = 0^\circ$ and 25° , simultaneously with the high-altitude peak of the northern polar latitudes, showing similar densities between 2×10^7 and 2×10^8 molecules/cm³. This high-altitude peak persists in location and intensity and location until $L_s = 45^\circ$. Unlike its counterpart in the north, this high-altitude peak does not dissipate after $L_s = 45^\circ$, but maintains high ozone densities over the 35–60-km altitude range between midsouthern fall and winter until $L_s = 180^\circ$. The high-altitude peak completely disappears throughout southern spring until midsouthern summer ($L_s = 330^\circ$). A newly formed high-altitude peak at the end of southern summer shows up at 60 km, with low ozone densities in the $3 \times 10^6\text{--}2 \times 10^7$ molecules/cm³ range, before gaining intensity at the beginning of the Martian year. The high-altitude peak in the south polar latitudes is more defined in season, and it is present for at least 60% of the year, showing similarities in location with its counterpart in the north during the first half of southern fall.

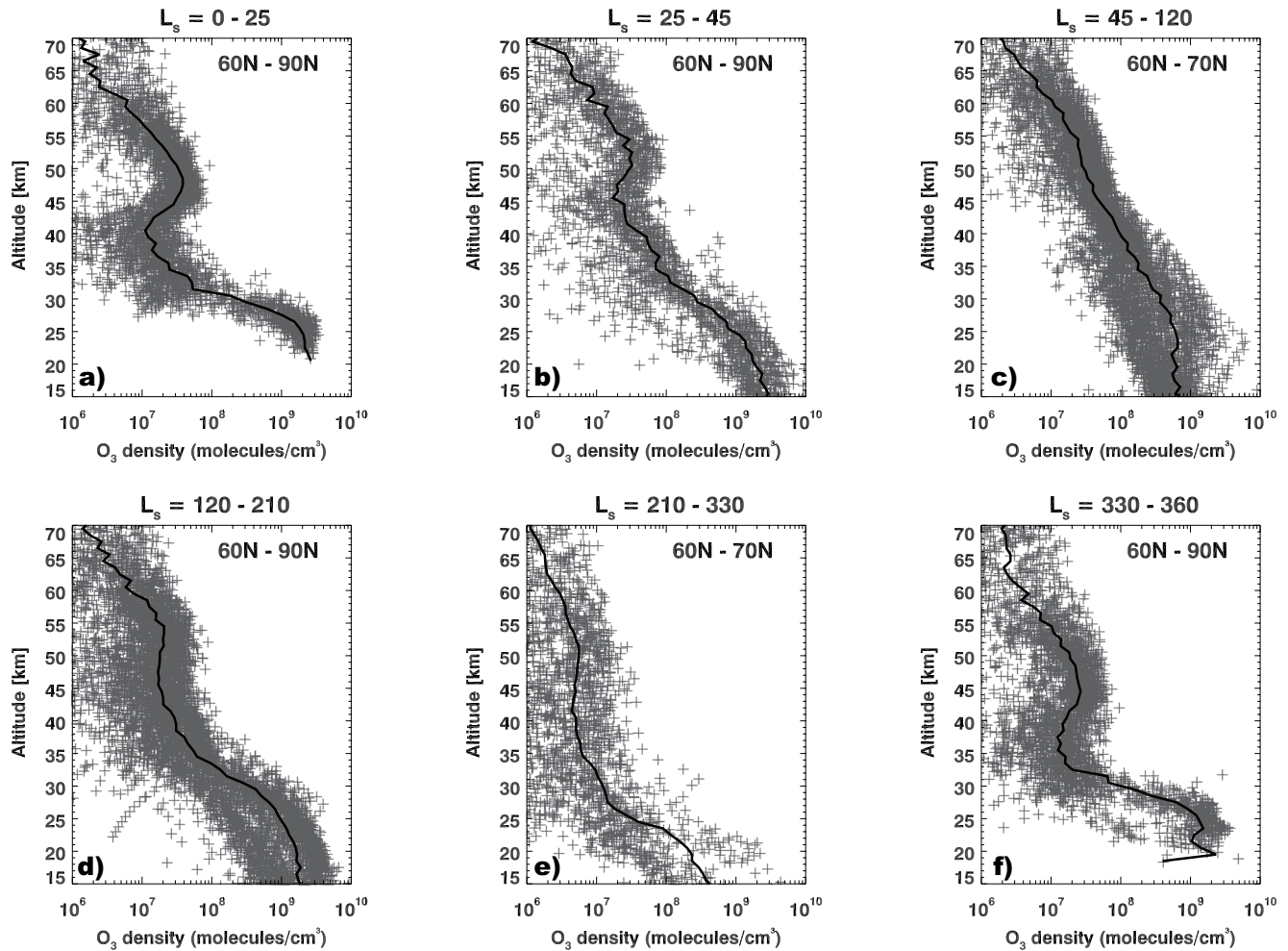


Figure 3. Vertical profiles of ozone over the north polar latitudes (60° – 88.7° N). This figure tracks the evolution of the vertical profile throughout an entire Martian year at several seasonal bins. The gray dots represent the ozone density ($\text{molecules}/\text{cm}^3$) as retrieved from each transmittance spectrum at the relevant tangent altitude (km). The black curve represents the average profile between 15 and 70-km altitude. The panels a, b, and c represent the vertical ozone profiles during the subseasonal bin $L_s = 0^{\circ}$ – 25° , $L_s = 25^{\circ}$ – 45° , and $L_s = 45^{\circ}$ – 120° , respectively. The panels d, e, and f represent the vertical ozone profiles during the subseasonal bin $L_s = 120^{\circ}$ – 210° , $L_s = 210^{\circ}$ – 330° , and $L_s = 330^{\circ}$ – 360° , respectively. As shown in Figure 1, the local time coverage for the ozone profiles shown here spans the various hours of the Martian sol. A high-altitude peak of ozone is detected over the north polar latitudes. The latitudinal range covered by ultraviolet and visible spectrometer (UVIS) is reduced to 60° – 70° N in the subseasonal bands $L_s = 45^{\circ}$ – 120° and 210° – 330° (panels c and e, respectively).

5.2. Latitudinal Evolution of the High-Altitude O_3 Peak in Seasonal Bands

Figure 5 shows the latitudinal distribution of the retrieved vertical O_3 abundance during four seasonal bands. Figure 5a shows this distribution around the beginning of northern spring at $L_s = 0^{\circ} \pm 45^{\circ}$. The high-altitude peak of O_3 is prominent in the northern hemisphere between latitudes 60° N and $\sim 85^{\circ}$ N, reaching densities on the order of 10^8 molecules/ cm^3 between altitudes 40 and 55 km, and has a counterpart in the southern hemisphere between latitudes 50° and $\sim 85^{\circ}$ S, with similar ozone densities between 40 and 55-km altitude. In the north, the minimum in O_3 between the high-altitude peak and the one near the surface shows abundances $<10^7$ molecules/ cm^3 , showing a complete separation between the two, with an order of magnitude lower densities in the high-altitude peak compared to the surface one. The high-altitude peaks disappear at midlatitudes in the south between 40° and 50° S and in the north around 55° N. A minimum in ozone abundances sets the boundaries between the high-altitude peaks at polar latitudes and a global enhancement in ozone ($\sim 10^8$ molecules/ cm^3) that exists in the lower atmosphere up to 50 km between 40° S and 30° N.

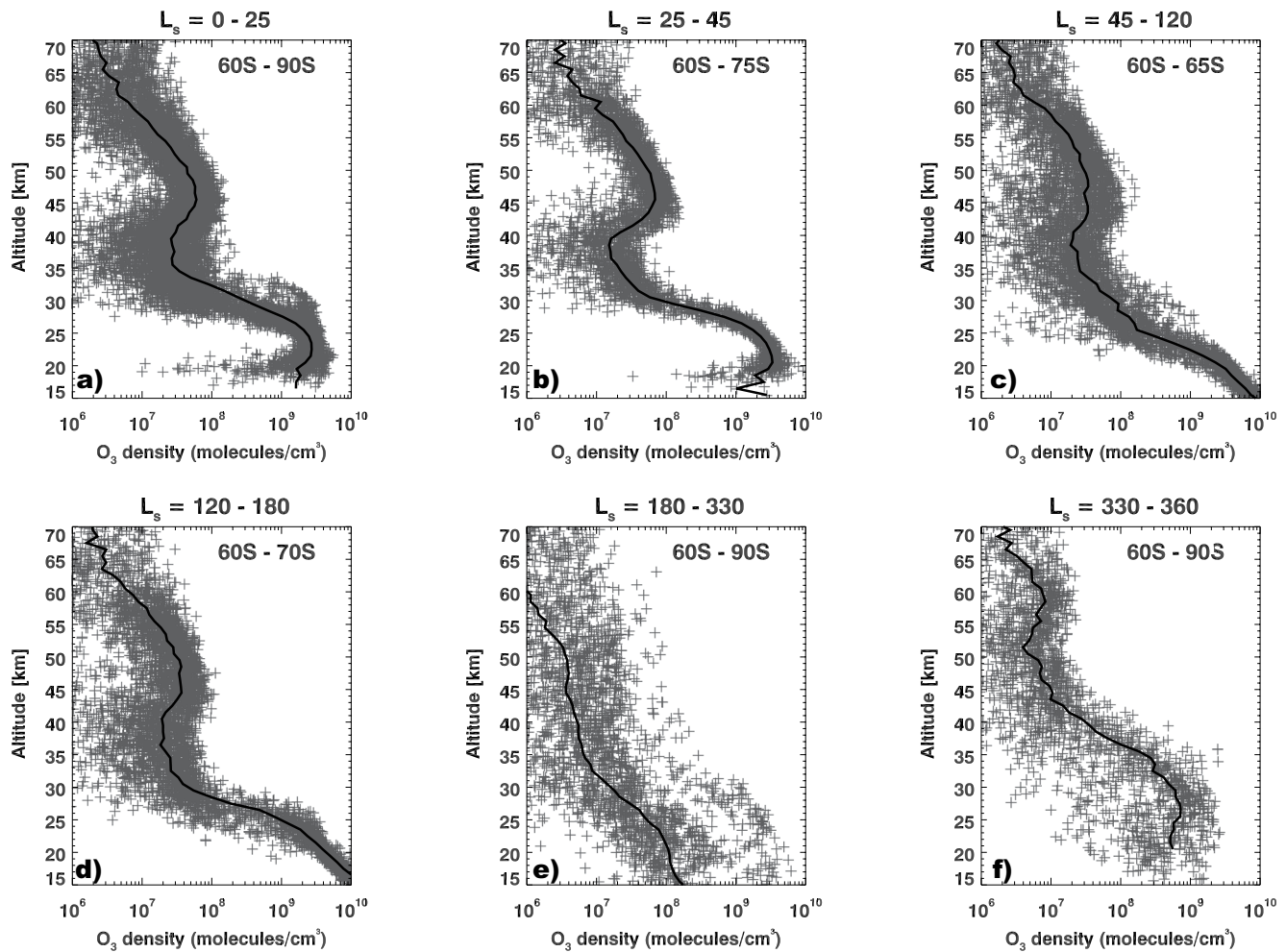


Figure 4. Vertical profiles of ozone over the south polar latitudes (60° – 83.4° S). This figure tracks the evolution of the vertical profile throughout an entire Martian year at several seasonal bins. The gray dots represent the ozone density ($\text{molecules}/\text{cm}^3$) as retrieved from each transmittance spectrum at the relevant tangent altitude (km). The black curve represents the average profile between 15 and 70-km altitude. The panels a, b, and c represent the vertical ozone profiles during the subseasonal bin $L_s = 0^{\circ}$ – 25° , $L_s = 25^{\circ}$ – 45° , and $L_s = 45^{\circ}$ – 120° , respectively. The panels d, e, and f represent the vertical ozone profiles during the subseasonal bin $L_s = 120^{\circ}$ – 180° , $L_s = 180^{\circ}$ – 330° , and $L_s = 330^{\circ}$ – 360° , respectively. A strong high-altitude peak of ozone is detected over the south polar latitudes.

At the beginning of northern summer at $L_s = 90^{\circ} \pm 45^{\circ}$ (Figure 5b), the polar latitudes are not covered by UVIS, but a low-altitude enhancement of ozone around 45° S is observed in the 25–35-km altitude range with densities at the 10^9 molecules/ cm^3 level. A high-altitude enhancement of ozone ($\sim 10^8$ molecules/ cm^3) is observed between 30° and 60° S; however, there is no counterpart to it within the UVIS coverage in the northern hemisphere below latitude 60° N.

The high-altitude peaks of ozone show up again at high latitudes around southern spring at $L_s = 180^{\circ} \pm 45^{\circ}$ (Figure 5c). The peak in the south shows up between 55° and 70° S in the altitude range 40–55 km, with ozone densities of 6 – 8×10^7 molecules/ cm^3 , but does not persist between 70° and 80° S. In contrast, the high-altitude peak of ozone in the north persists between 60° and 85° N and is located in the altitude ranges 45–55, 55–60, and 45–55 km, at latitudes ranges 60° – 75° N, 75° – 85° N, and $>85^{\circ}$ N, respectively, with ozone densities in the upper 10^7 molecules/ cm^3 . The polar latitudes were not covered by UVIS in the southern summer at $L_s = 270^{\circ} \pm 45^{\circ}$ (Figure 5d). Within the observed latitudinal range 50° – 65° S and 50° – 65° N where the data are not sparse, no distinct high-altitude peaks of ozone were observed, and the ozone is uniformly distributed above 30 km.

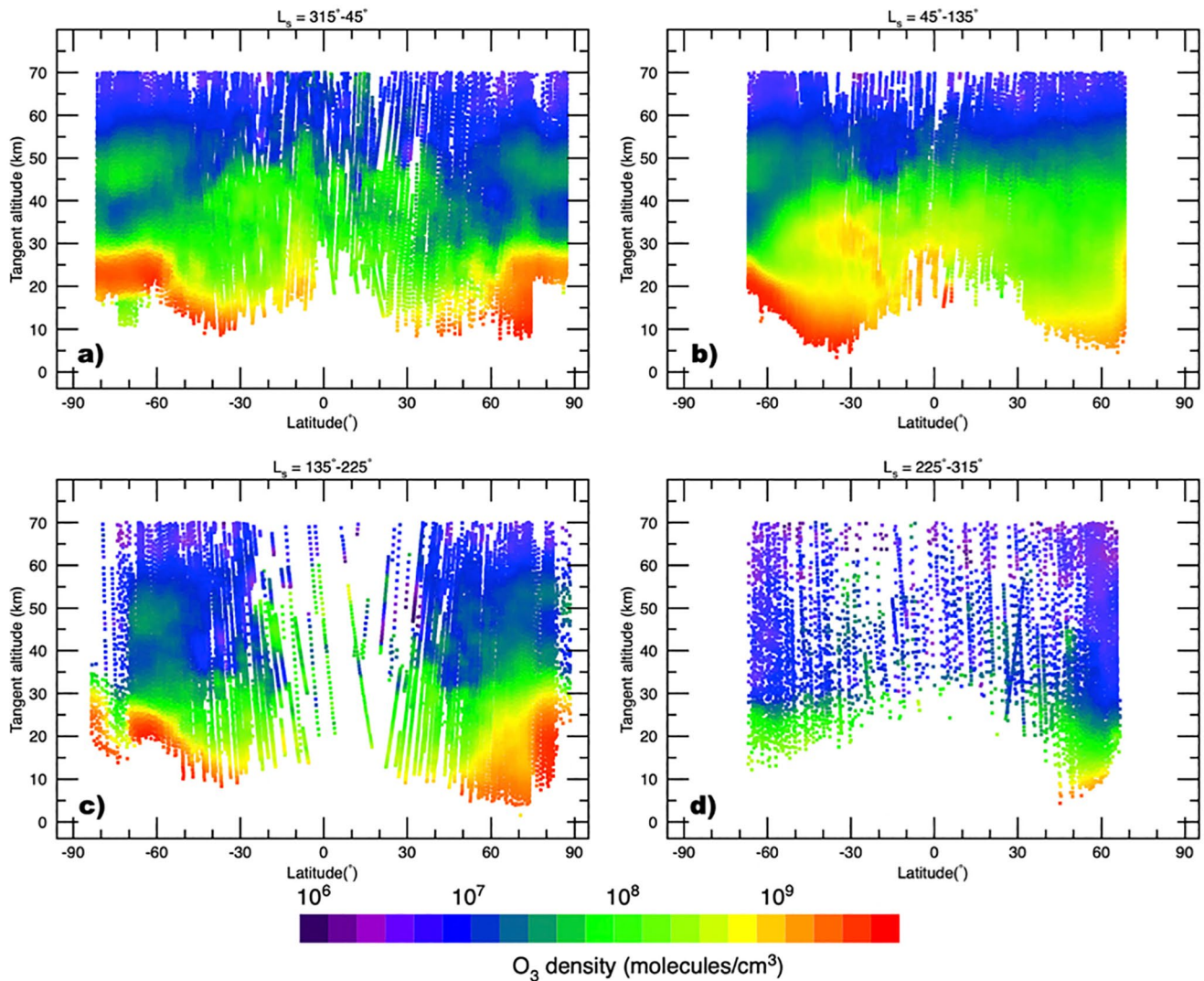


Figure 5. Latitudinal distribution (90°S–90°N) of the retrieved vertical O₃ density (molecules/cm³) below 70-km altitude at four subseasonal bands. The results are shown after applying a two-dimensional convolution of $\Delta\text{latitude} = 5^\circ$ in the latitudinal dimension (x axis) and $\Delta z = 3$ km in the altitude dimension (y axis). Panel a shows the vertical distribution of ozone centered at the beginning of northern spring in the L_s range 315°–45°. Panel b shows the vertical distribution of ozone at the beginning of northern summer in the L_s range 45°–135°. Panel c shows the vertical distribution of ozone at the beginning of southern spring in the L_s range 135°–225°. Panel d shows the vertical distribution of ozone at the beginning of southern summer in the L_s range 225°–315°.

5.3. Seasonal Evolution of the High-Altitude O₃ Peak in Latitude Bands

The seasonal distribution of the vertical abundance of ozone is shown in Figure 6. The high-altitude peak of ozone is observed above the north polar latitudes during most of the seasonal coverage provided by UVIS (Figure 6a), with maximum abundances reaching 8×10^7 molecules/cm³ during northern spring.

In the latitude range 60°–70°N (Figure 6b), the high-altitude peak of ozone is well observed during northern spring until $L_s = 40^\circ$, with densities above 10^8 molecules/cm³. The enhancement of ozone around 40-km altitude in Figure 6b fills the minimum in ozone between the high-altitude peak and the main ozone layer near the surface of Mars, making the high-altitude peak disappear between midnorthern spring ($L_s > 40^\circ$) until midnorthern summer at $\sim L_s = 130^\circ$. The high-altitude peak reemerges and lasts until the beginning of southern spring, but it is limited in its vertical extent (< 10 km) and intensity, with densities $< 10^7$ molecules/cm³. Throughout the rest of the Martian year (Figure 6b), the ozone is depleted at the altitudes of the high-altitude peak before the reappearance of the peak right before the end of northern winter at $L_s = 355^\circ$.

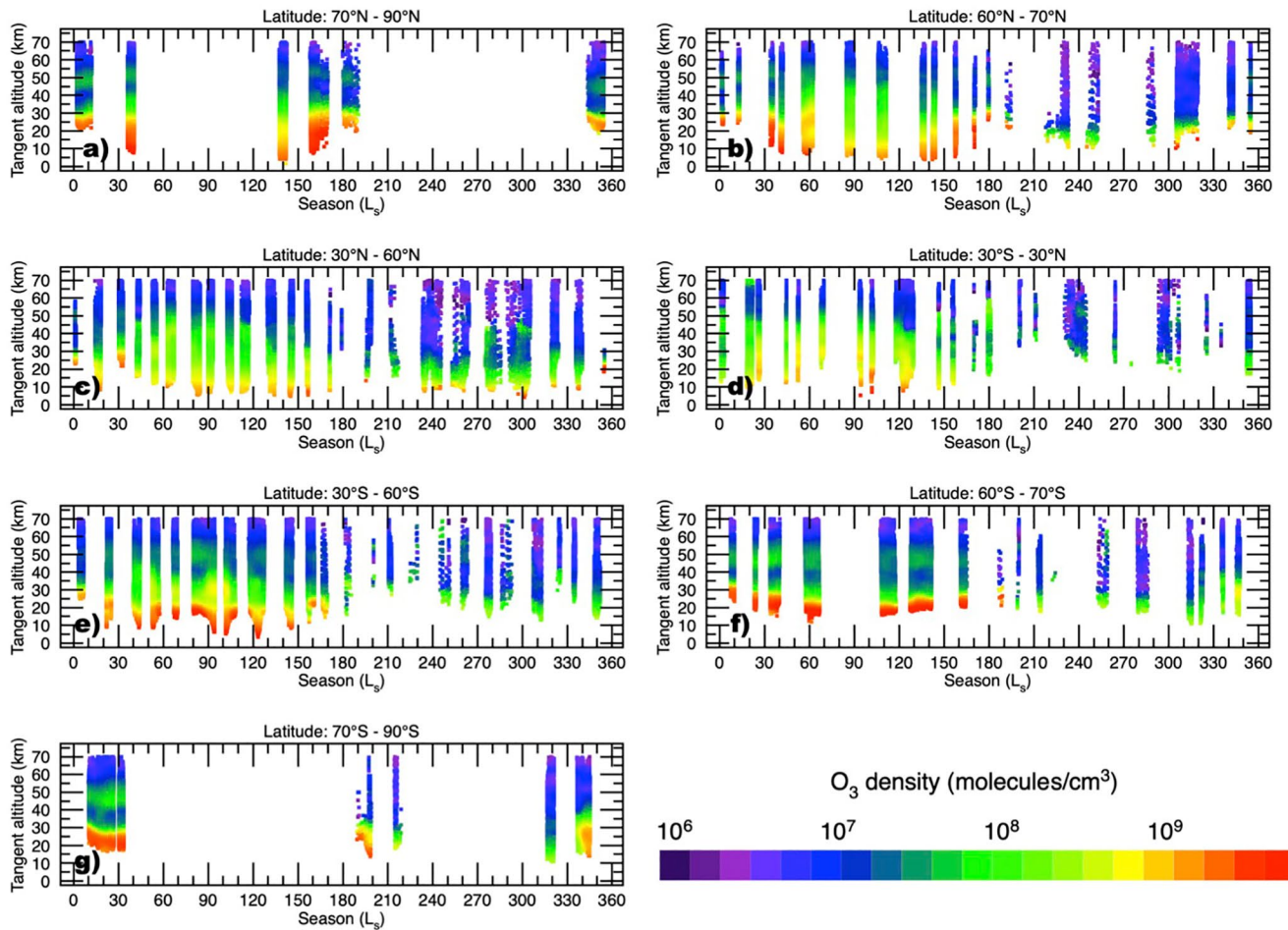


Figure 6. Seasonal distribution ($L_s = 0\text{--}360^\circ$) of the retrieved vertical O_3 density ($\text{molecules}/\text{cm}^3$) below 70-km altitude at seven latitude bands. The results are shown after applying a two-dimensional convolution of $\Delta L_s = 5^\circ$ in the seasonal dimension (x axis) and $\Delta z = 3$ km in the altitude dimension (y axis). Panel a represents the vertical distribution of ozone at different local time coverage (spanning the various hours of the Martian sol as shown in Figure 1) at high northern latitudes between 70° and 90°N . Panel b represents the distribution between 60° and 70°N . Panel c represents the distribution between 30° and 60°N . Panel d represents the vertical distribution of ozone over the equator ($30^\circ\text{S}\text{--}30^\circ\text{N}$) due to the low frequency of ultraviolet and visible spectrometer (UVIS) observations around the equator. Panel e represents the distribution between 30° and 60°S . Panel f represents the vertical distribution of ozone at high southern latitudes between 60° and 70°S where a strong high-altitude peak of ozone is observed. Panel g represents the vertical distribution of ozone at polar latitudes between 70° and 90°S in the south where the strong high-altitude peak of ozone persists.

The high-altitude peak disappears for most of the Mars year at midnorthern latitudes (Figure 6c), and emerges around midnorthern spring ($L_s \sim 30^\circ$) with abundances of 5×10^7 molecules/ cm^3 . Due to the lack of UVIS coverage of the equatorial regions, we combined the ozone distribution between 30°S and 30°N (Figure 6d). There is no major presence of the high-altitude peak of ozone around the equator throughout the entire Martian year. At midsouthern latitudes (Figure 6e), the peak shows up at the end of southern fall and early winter between $L_s \sim 80^\circ\text{--}130^\circ$. In contrast, a very well-defined high-altitude peak of ozone is present over southern latitudes between 60° and 70°S (Figure 6f), with maximum densities surpassing 10^8 molecules/ cm^3 in southern fall, and it remains throughout southern fall and winter, before completely disappearing for the rest of the Martian year. In the south polar latitudes (Figure 6g), the peak is very strong ($>10^8$ molecules/ cm^3) during southern fall between $L_s = 10^\circ$ and 30° . Compared to the north, the latitudinal extent of the high-altitude peak of ozone is larger in the southern latitudes as it can be present at as low as 30°S .

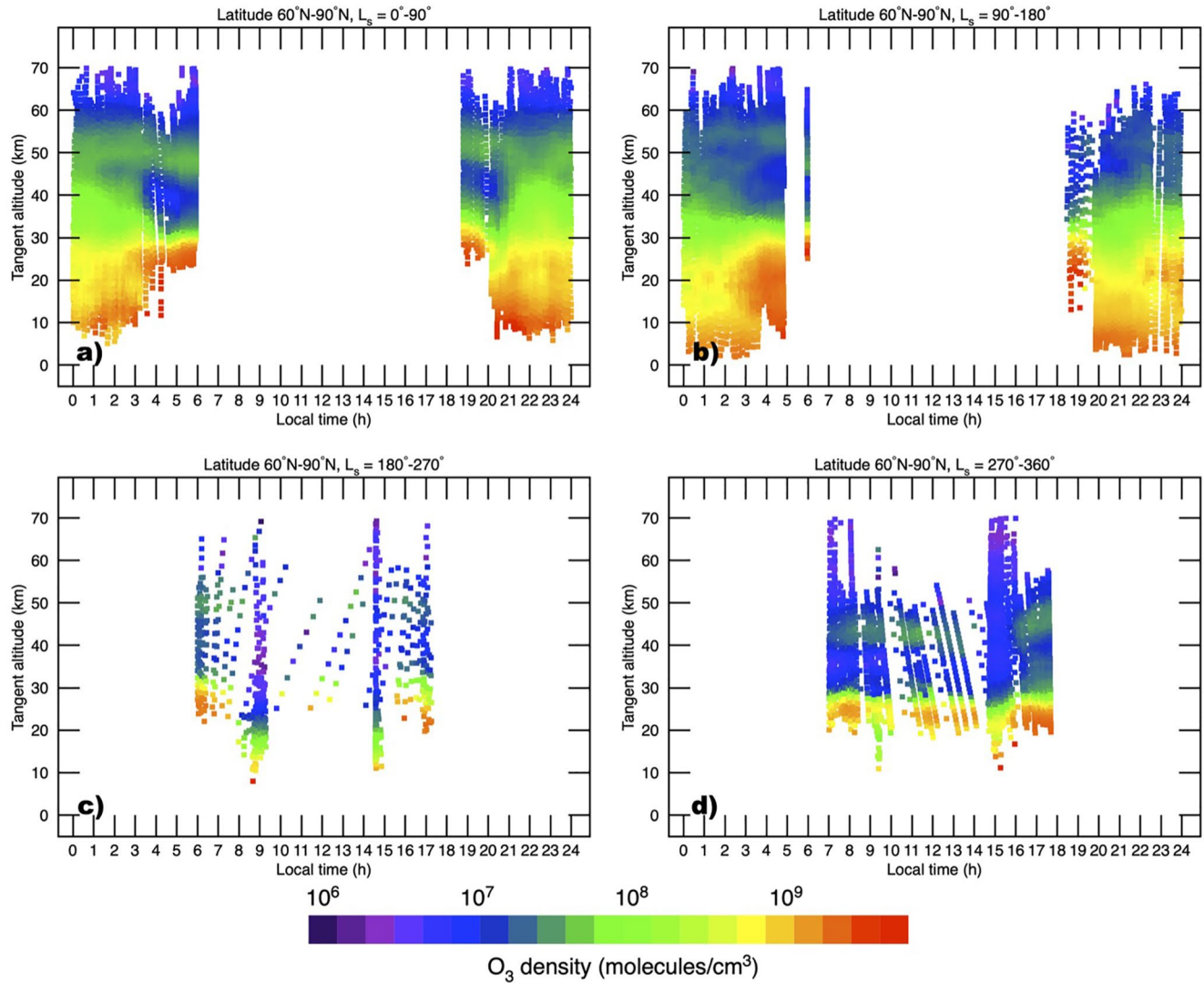


Figure 7. Vertical distribution of the retrieved O_3 abundance (molecules/ cm^3) below 70-km altitude at four seasons on Mars using sunrise and sunset occultations, over the north polar latitudes (60° – 90°N). The results are shown after applying a two-dimensional convolution of $\Delta\text{LT} = 1$ h in the local time dimension (x axis) and $\Delta z = 3$ km in the altitude dimension (y axis). Panels a and b represent the local time distribution of ozone during northern spring and summer seasons, respectively. Panels c and d represent the local time distribution of ozone during southern spring and summer seasons, respectively. The high-altitude peak of ozone is still observed during daytime.

5.4. The High-Altitude O_3 Peak During Sunrise/Sunset Occultations

The coverage of the UVIS solar occultation observations provides a window into the evolution of the vertical distribution of ozone and yields important information on the efficiency of the photochemical production/destruction of high-altitude ozone (e.g., Daerden et al., 2019; Lefèvre et al., 2004; Montmessin & Lefèvre, 2013).

By definition, the geometry of a solar occultation only allows observations at locations transitioning between daylight and night. Most of the time, these solar occultations are at either local sunrise or at sunset. Observations at sunrise observe the part of the atmosphere that has just emerged into sunlight after being in darkness during the night, while observations at sunset observe the atmosphere that has been in sunlight all day. At polar latitudes the observations can also sample the transition between areas in polar night and daylight, or between areas with 24 hr daylight and night. In the figures described below, we plot retrieved ozone profiles as a function of local time to separate the cases of sunrise, sunset, and polar observations.

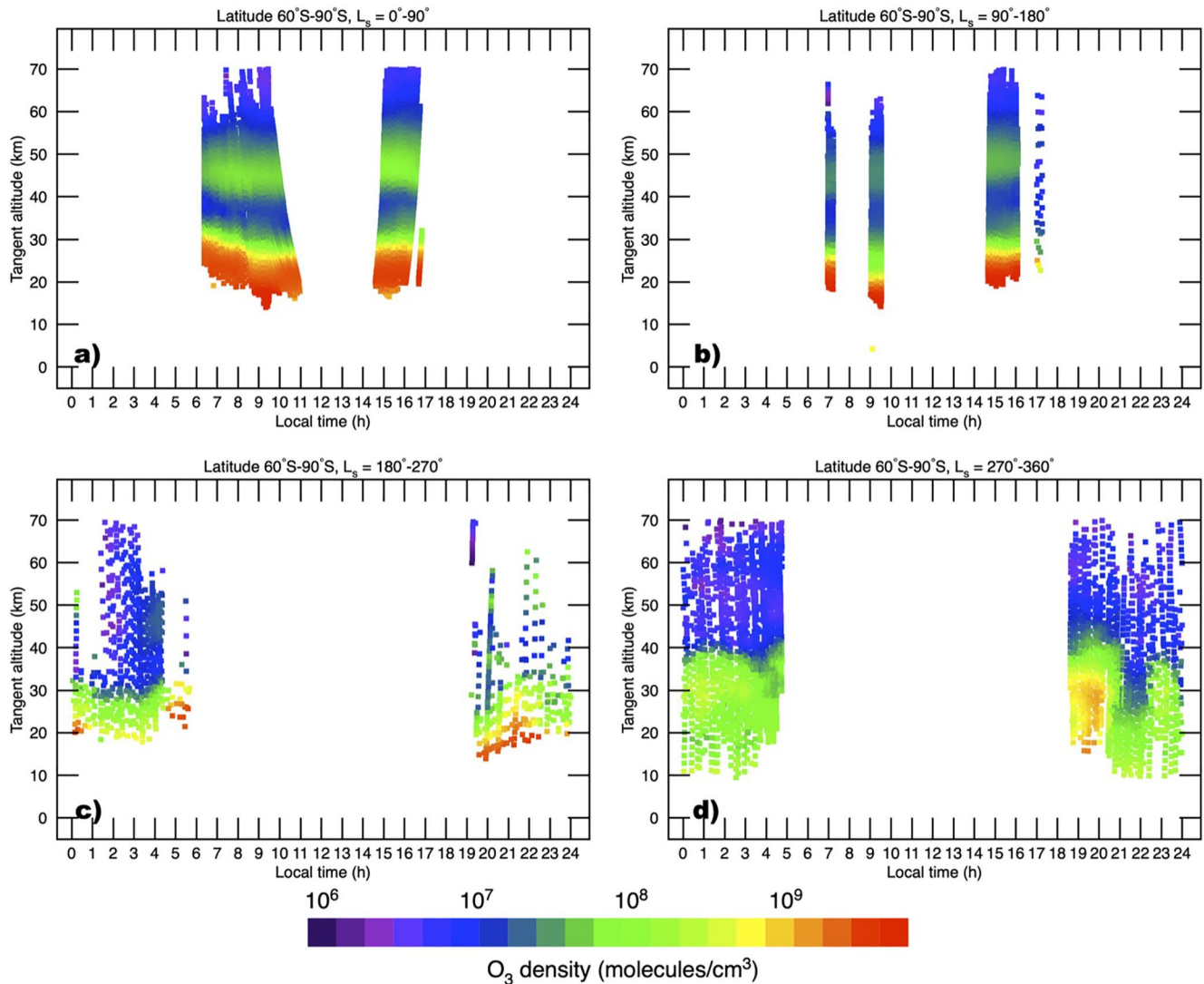


Figure 8. Vertical distribution of the retrieved O_3 abundance (molecules/cm³) below 70-km altitude at four seasons on Mars, over the south polar latitudes (60°–90°S) using sunrise and sunset occultations. The results are shown after applying a two-dimensional convolution of $\Delta LT = 1$ h in the local time dimension (x axis) and $\Delta z = 3$ km in the altitude dimension (y axis). Panels a and b represent the local time distribution of ozone during southern fall and winter seasons, respectively. Panels c and d represent the local time distribution of ozone during southern spring and summer seasons, respectively. The high-altitude peak of ozone is prominently observed during the southern fall and winter seasons.

Figure 7 shows the vertical profile of ozone over the north polar latitudes during four seasons on Mars. During northern spring (Figure 7a), the north polar region is illuminated, and the high-altitude peak of ozone between 45 and 60-km altitude persists and maintains abundances $>10^8$ molecules/cm³. During northern summer (Figure 7b), the high-altitude peak of ozone is located between 50 and 60-km altitude, but with low abundances ($\sim 6 \times 10^7$ molecules/cm³) compared to northern spring. The peak remains a distinct entity from the near-surface enhancement of ozone. At southern spring and summer seasons (Figures 7c and 7d), the high-altitude peak of ozone is observed between 40 and 55-km altitude with ozone abundances not exceeding 10^8 molecules/cm³.

Over the south polar latitudes, the high-altitude peak of ozone persists during southern fall (Figure 8a). The vertical location is maintained between 40 and 60-km altitude, as well as the abundance ($\sim 5 \times 10^8$ molecules/cm³). The same pattern is observed around southern winter (Figure 8b), but with lower abundances of ozone in the high-altitude peak ($<10^8$ molecules/cm³). The sunrise and sunset occultations both show

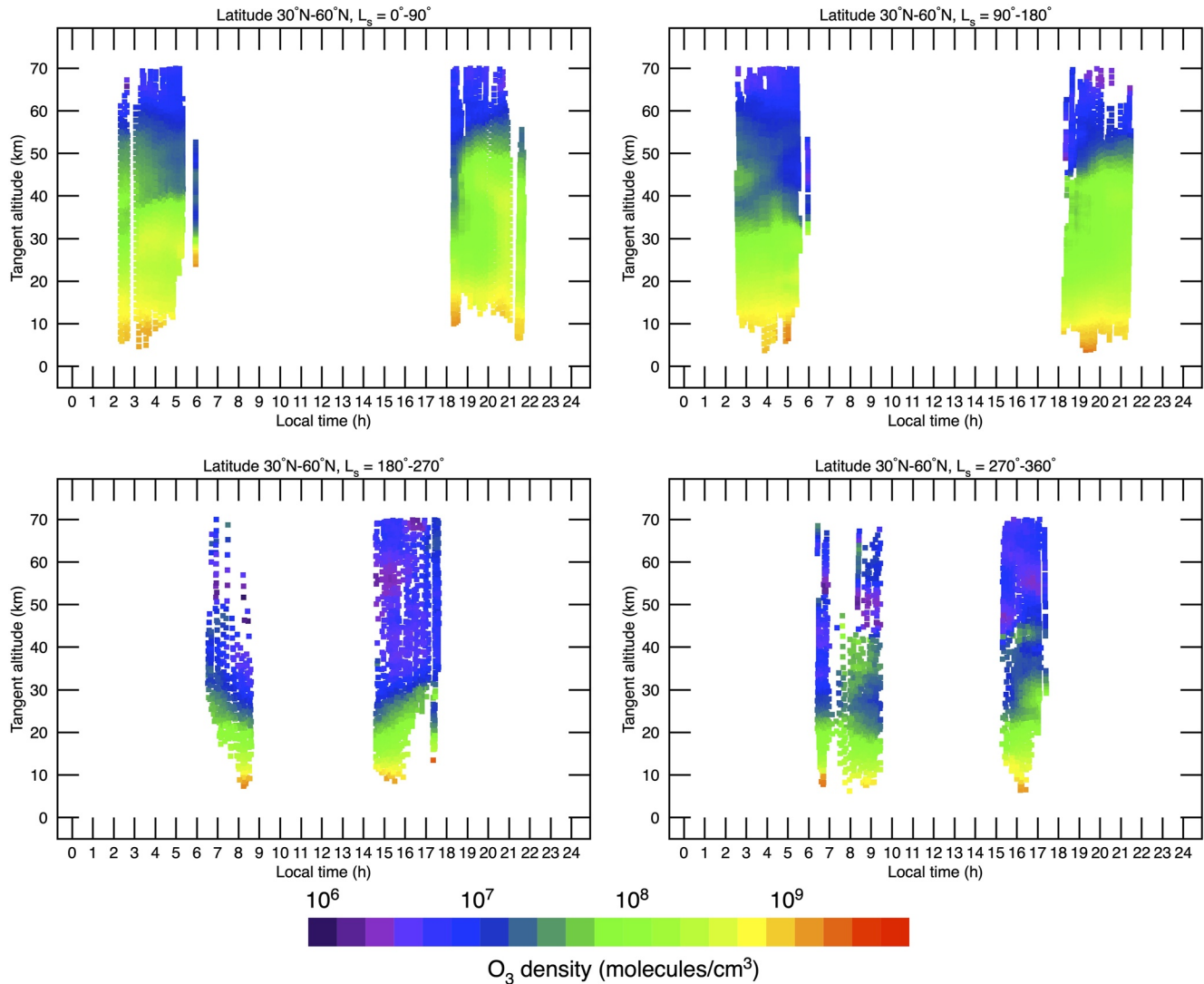


Figure 9. Vertical distribution of the retrieved O_3 abundance (molecules/cm³) below 70-km altitude at four seasons on Mars, over the midlatitudes in the north (30°–60°N) using sunrise and sunset occultations. The results are shown after applying a two-dimensional convolution of $\Delta LT = 1$ h in the local time dimension (x axis) and $\Delta z = 3$ km in the altitude dimension (y axis). Panels a and b represent the local time distribution of ozone during northern spring and summer seasons, respectively. Panels c and d represent the local time distribution of ozone during southern spring and summer seasons, respectively. There is no clear presence of the high-altitude peak of ozone.

the high-altitude peak of ozone, indicating that the peak could persist throughout the day. The high-altitude peak of ozone is present in Figures 8a and 8b on the day side, and it disappears in Figures 8c and 8d on the night side. The presence of water vapor in the atmosphere on the night side in Figures 8c and 8d could explain the low ozone abundance in the altitude range 40–60 km (see Patel et al., 2021 for the climatology of ozone and its anticorrelation with water vapor).

Figure 9 shows the vertical distribution of ozone from sunrise and sunset occultations in the midlatitude range (30°–60°N). The high-altitude peak of ozone is almost nonexistent, and the ozone abundances show an increase at high altitudes due to the decrease in the hygropause altitude at this time of the year (Clancy & Nair, 1996).

During northern spring around midlatitudes in the south (30°–60°S), the high-altitude peak of ozone is still observed (Figure 10a), but with low ozone abundances ($<10^8$ molecules/cm³), contrary to its counterpart in the north that is almost nonexistent around this season. More ozone around 40 km is present in the sunset

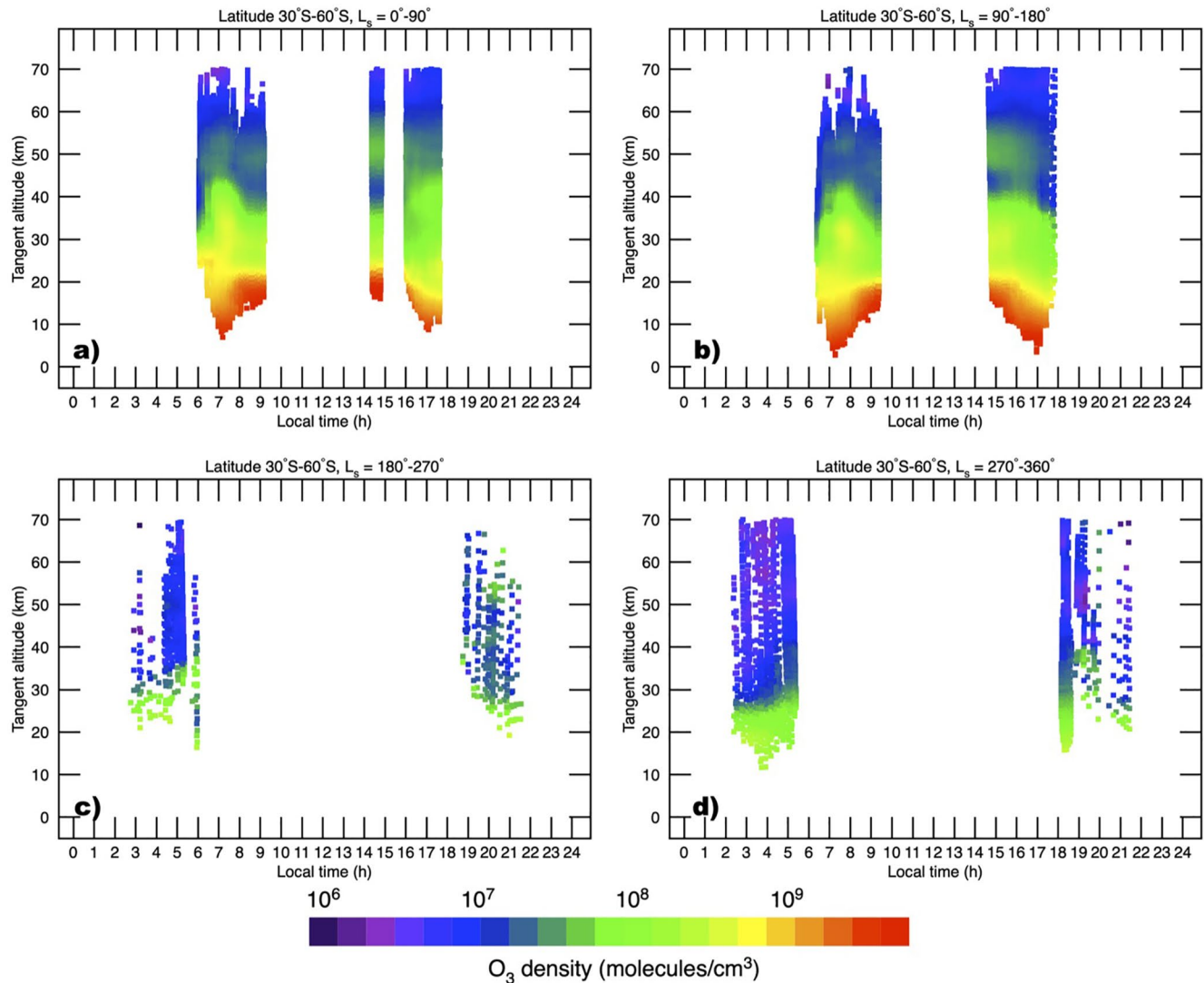


Figure 10. Vertical distribution of the retrieved O_3 abundance (molecules/cm³) below 70-km altitude at four seasons on Mars, over the midlatitudes in the south (30°–60°S) using sunrise and sunset occultations. The results are shown after applying a two-dimensional convolution of $\Delta LT = 1$ h in the local time dimension (x axis) and $\Delta z = 3$ km in the altitude dimension (y axis). Panels (a and b) represent the local time distribution of ozone during southern fall and winter seasons, respectively. Panels (c and d) represent the local time distribution of ozone during southern spring and summer seasons, respectively. There is no clear presence of the high-altitude peak of ozone during southern spring and summer seasons.

occultations, filling the minimum in ozone between the surface layer of ozone and the high-altitude peak. The peak persists during southern winter (Figure 10b), but it becomes weak during sunrise occultations. During southern spring and summer seasons, the high-altitude peak shows no appearance in the solar occultations.

Due to the scarcity of observations around equatorial latitudes, the ozone distribution presented in Figure 11 shows results for latitudes between 30°S and 30°N. The high-altitude peak of ozone no longer exists independently at equatorial latitudes. During southern spring and summer (Figures 11c and 11d), the ozone becomes depleted above 40 km in the sunset occultations.

Piccialli et al. (2021) investigated the impact of gradients in ozone concentration along the line-of-sight on the retrieval of ozone under sunrise/sunset conditions using eight SPICAM-UV solar occultations observations taken between June and August 2004 (MY27). The impact of gradients on the retrievals strongly follows the GEM model results (Daerden et al., 2019; Neary & Daerden, 2018) used here in Section 5.6.

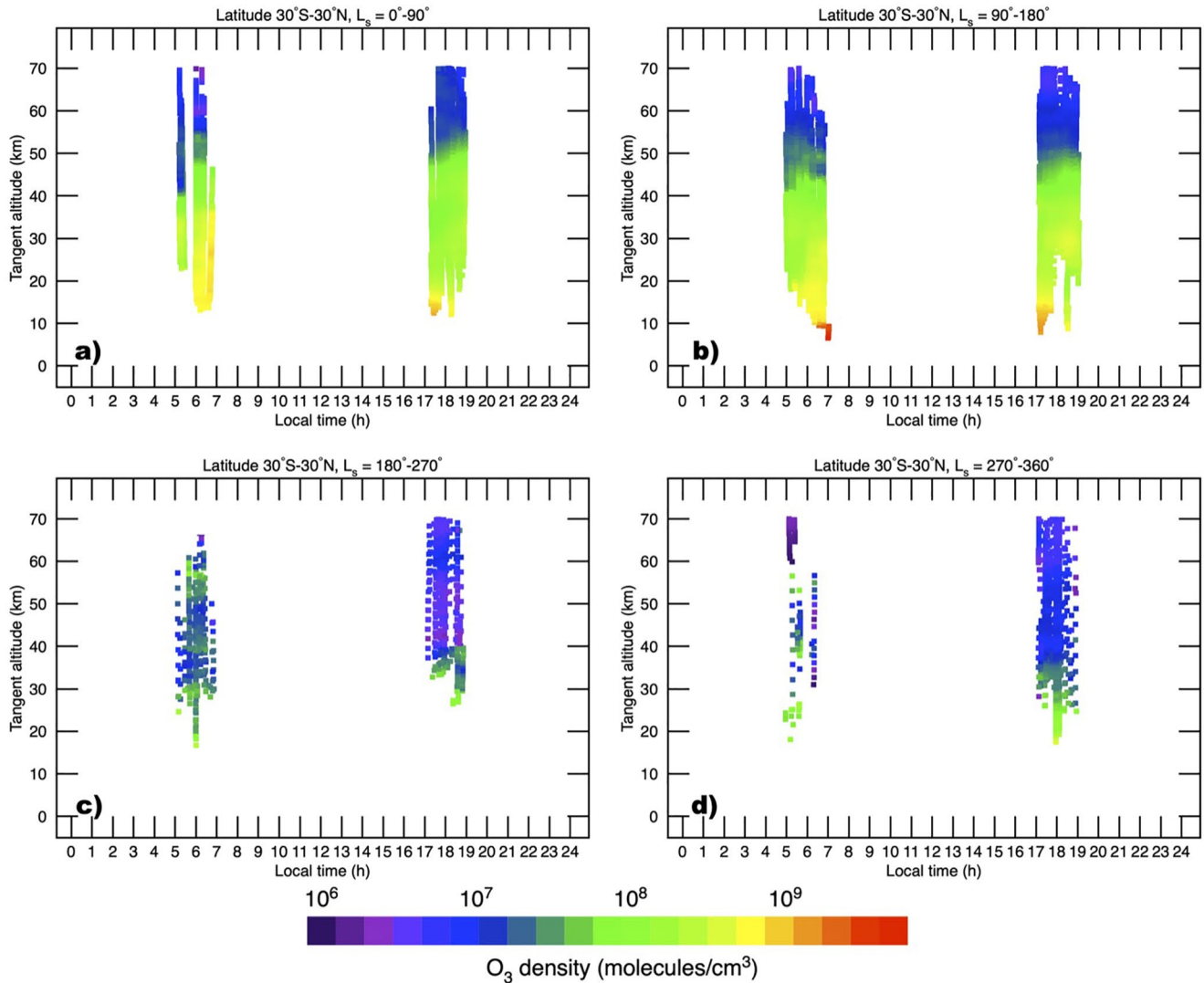


Figure 11. Vertical distribution of the retrieved O₃ abundance (molecules/cm³) below 70-km altitude at four seasons on Mars, over the equatorial latitudes (30°S–30°N) using sunrise and sunset occultations. The results are shown after applying a two-dimensional convolution of $\Delta t = 1$ h in the local time dimension (x axis) and $\Delta z = 3$ km in the altitude dimension (y axis). Panels a and b represent the local time distribution of ozone during northern spring and summer seasons, respectively. Panels c and d represent the local time distribution of ozone during southern spring and summer seasons, respectively. There is no clear presence of the high-altitude peak of ozone.

5.5. Evolution of the High-Altitude O₃ Peak on the Hemispheric Scale

The most complete picture of the vertical distribution of ozone over a full Mars year is presented in Figure 12, where its seasonal evolution is shown in both hemispheres. The high-altitude peak in the northern hemisphere pertaining to latitudes $>50^\circ\text{N}$ is present until $L_s = 40^\circ$ (Figure 12, upper panel). Later in the season the produced ozone from below 45-km altitude fills the minimum in ozone between the high-altitude layer and the surface layer until midnorthern summer at $L_s = 130^\circ$. The high-altitude peak of ozone reemerges again as a distinct layer until the end of northern summer. The peak over high latitudes completely disappears throughout northern fall and most of winter before forming again at $L_s = 340^\circ$.

The high-altitude ozone peak is more prominent in the southern hemisphere (Figure 12, lower panel), and is attributed to latitudes poleward of 30°S. This layer maintains altitude and intensity throughout southern fall and winter seasons until $L_s = 170^\circ$. The enhancement in the ozone abundance around $L_s = 50^\circ, 90^\circ,$ and 120° in the altitude range 30–40 km, below the high-altitude peaks of ozone, is attributed to the low latitudes between 30° and 60°S. The high-altitude peak of ozone in the southern hemisphere completely

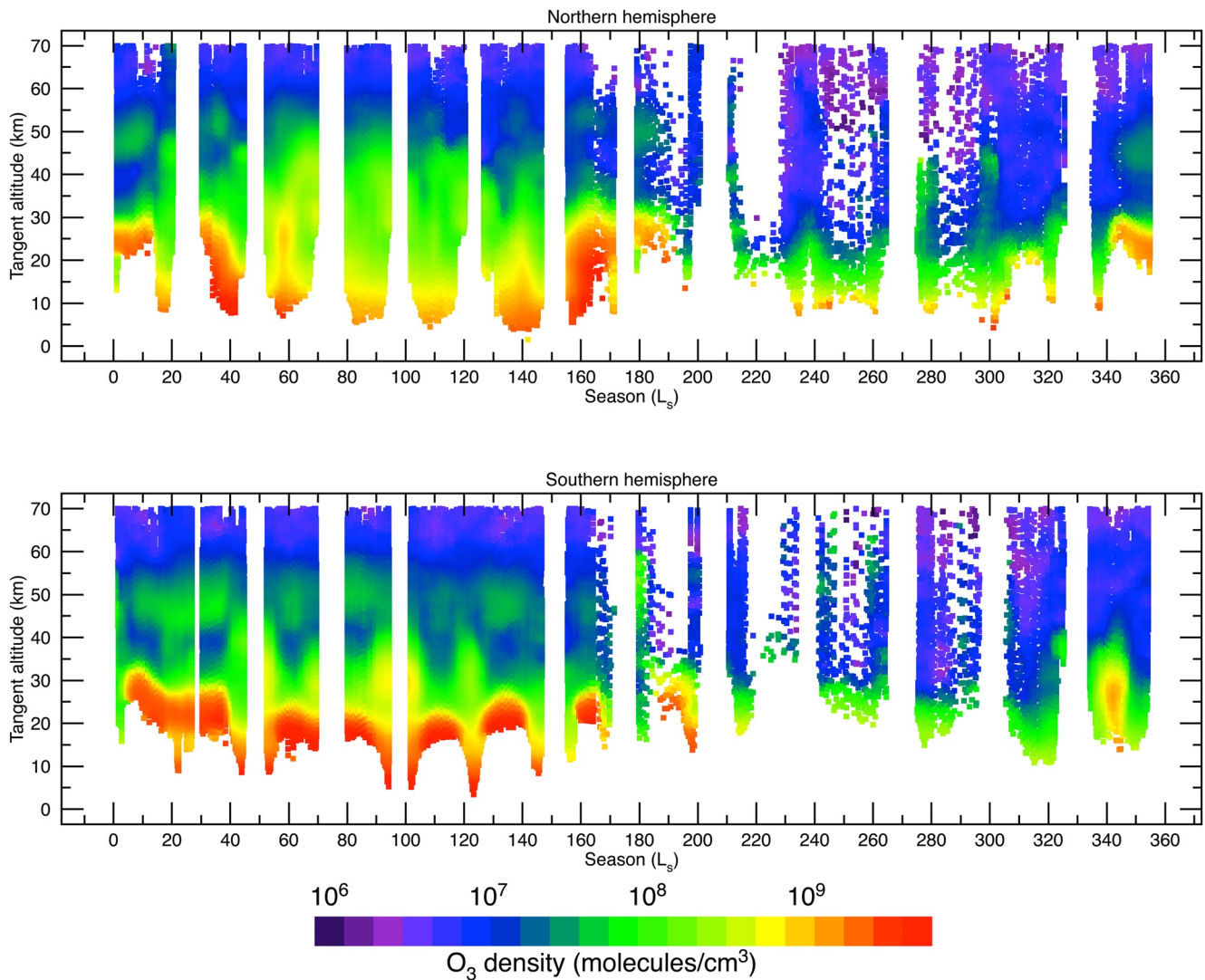


Figure 12. Seasonal distribution of the retrieved vertical O_3 abundance (molecules/cm³) in the northern (upper panel) and southern (lower panel) hemispheres. The results are shown after applying a two-dimensional convolution of $\Delta L_s = 5^\circ$ in the local time dimension (x axis) and $\Delta z = 3$ km in the altitude dimension (y axis). The high-altitude peaks of ozone are visible in both hemispheres during northern spring (southern fall).

disappears throughout the rest of the Martian year, leaving the atmosphere depleted of ozone above 40-km altitude over the high latitudes in the southern hemisphere.

5.6. Comparisons With the GEM Model Results

The vertical distribution of ozone as a function of latitude in seasonal bands as modeled by GEM-Mars is shown in Figure 13. To allow a one-to-one comparison with the UVIS retrievals, the GEM-Mars O_3 abundance values are given at the same altitude, longitude, latitude, local time, and L_s at each UVIS observation. During the beginning of northern spring (Figure 13a), the GEM-Mars results very well reproduce the general behavior of ozone in the atmosphere as observed by the UVIS retrievals, especially with the enhancement of ozone above 35 km. The main difference is that GEM predicts large amounts of ozone over the entire 35 and 55-km altitude range, with values in the 5×10^7 – 2×10^8 molecules/cm³ range at polar latitudes. In contrast, the values from UVIS retrievals show similar abundance values of a few times 10^8 molecules/cm³ but over a smaller vertical range in the atmosphere between altitudes 40 and 55 km. This can be explained by deviations of the simulated water vapor profile (Aoki et al., 2019) mostly caused by the simple treatment of

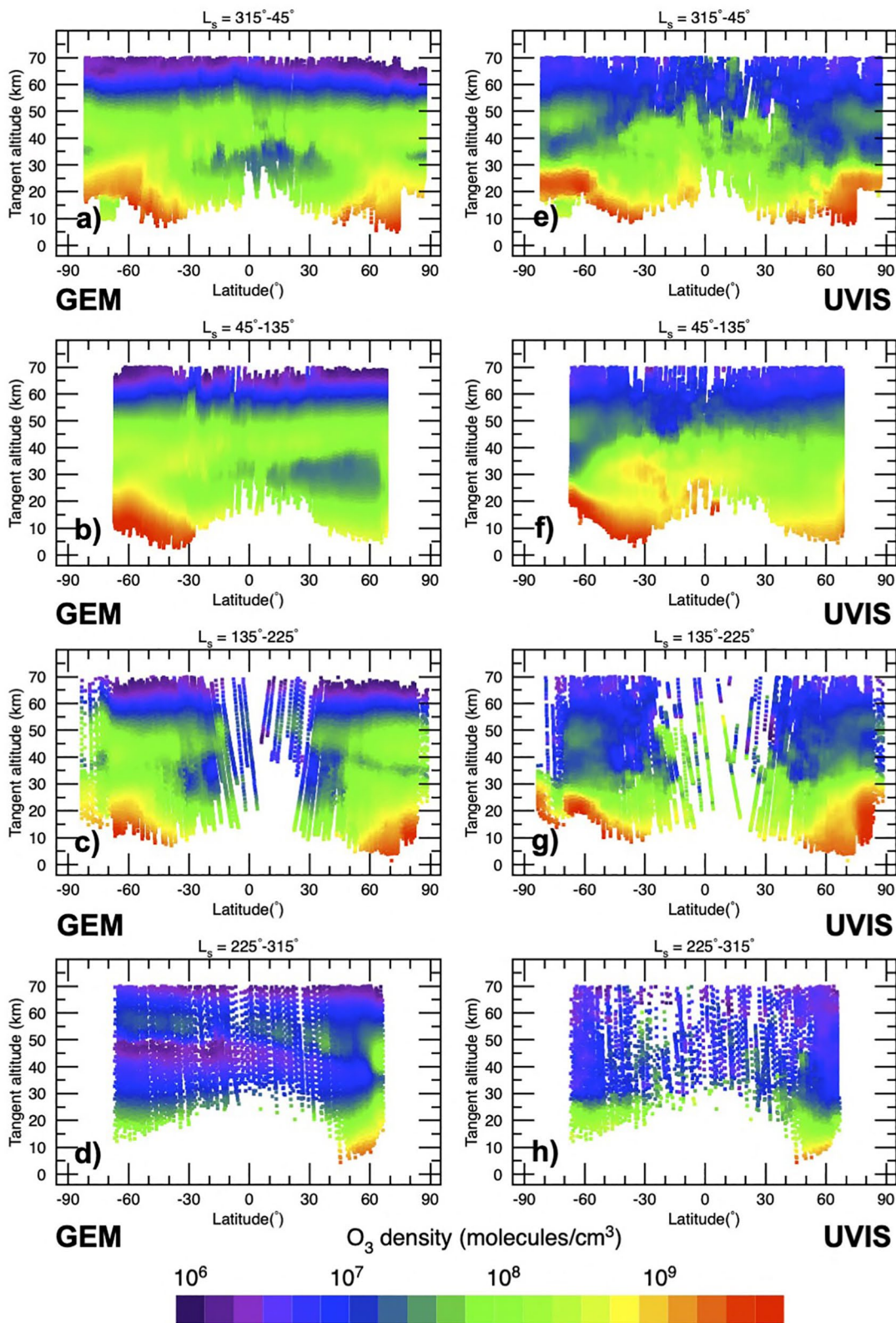


Figure 13.

water ice clouds in GEM-Mars. In Aoki et al. (2019, Figure 8c), it is shown that GEM-Mars underestimates the water vapor abundances at the locations of the high-altitude ozone peak, causing the model to form more ozone than observed.

Around the beginning of northern summer at $L_s = 90^\circ \pm 45^\circ$ (Figure 13b), the high ozone abundances below 40-km altitude over the midlatitudes in the south are in good agreement with the UVIS retrievals. However, GEM-Mars predicts a distinct high-altitude peak of O_3 between 40 and 50 km, with a minimum in ozone between 20 and 40-km altitude over the midlatitudes in the north, whereas UVIS retrievals show a continuous enhancement in the ozone abundances beginning at 60-km altitude and gradually decreasing with height. As was shown and discussed in Daerden et al. (2019), the current GEM model simulates higher water abundances than observed in the aphelion season because of the presence of the aphelion cloud belt and imperfectly simulated cloud radiative effects (e.g., Daerden et al., 2019, Figures 15, 16, and 28). The excess in water vapor between $L_s = 60^\circ$ and 100° shown in Figure 15 in Daerden et al. (2019) can be considered as the direct cause of the low ozone abundances shown in Figure 13b. Indeed, the impact of water vapor abundances on ozone is very strong and immediate (Daerden et al., 2019; Lefèvre et al., 2004).

The extent and magnitude of the high-altitude enhancement of ozone at polar latitudes in the north and south are repeated in the GEM-Mars results around the beginning of southern spring at $L_s = 135^\circ$ – 225° (Figure 13c). The general behavior of vertical ozone with the high-altitude peak is well reproduced, but the GEM results show average abundances around 10^8 molecules/cm³, peaking in the 40–45-km altitude range whereas UVIS retrievals have lower abundance of around 5×10^7 molecules/cm³, peaking around 50 and 55-km altitudes. The explanation is very similar to before, i.e., resulting from the low water abundances in GEM-Mars compared to NOMAD water observations (Aoki et al., 2019, Figure 6a) at the location of the ozone peak.

The GEM-Mars simulations share similar results with UVIS retrievals, indicating depleted ozone abundance values over 25-km altitude around the beginning of southern summer at $L_s = 225^\circ$ – 315° (Figure 13d). A slight enhancement in ozone between 45 and 55-km altitude is seen in the GEM simulations around 60° N. The simulated depletion is a result of excessive water vapor simulated in the 25–50-km altitude range at southern altitudes in this season (Aoki et al., 2019, Figure 6e).

The full seasonal distribution of the vertical abundance of ozone using GEM-Mars simulations in the northern and southern hemispheres is shown in Figure 14. In the northern hemisphere (Figure 14a), the high-altitude ozone peak is well described in the GEM-Mars simulations, especially during northern summer. The ozone enhancement above the minimum at 35-km altitude between $L_s = 0^\circ$ and 10° , as well as between 40 and 45-km altitude between $L_s = 60^\circ$ and 70° , both in abundance and location. The high-altitude abundances of ozone below 55 km are also well in agreement with the UVIS retrievals during northern summer, but a difference between GEM-Mars and UVIS retrievals is observed between 20 and 30-km altitude between $L_s = 80^\circ$ and 140° , showing a depletion in the O_3 abundances in the GEM-Mars results.

This readily results from issues with the simulation of water vapor abundances in the aphelion season, related to radiative effects of clouds in the aphelion cloud belt, as was extensively discussed in Daerden et al. (2019). The high-altitude peak between $L_s = 160^\circ$ and 170° is well reproduced by GEM-Mars, but it presents higher abundances peaking at 8×10^8 molecules/cm³, exceeding ~ 8 times the peak values by the UVIS retrievals. This is related to the low water vapor abundances simulated in GEM in the higher altitudes/high latitude regions, as shown in Daerden et al. (2019) and Aoki et al. (2019). The GEM-Mars simulations predict high-altitude peaks in O_3 abundances around $L_s = 220^\circ$ and between $L_s = 280^\circ$ and 360° with various abundances and vertical extents. However, the UVIS retrievals did not detect similar isolated

Figure 13. Global Environmental Multiscale (GEM)-Mars model simulation of ozone vertical abundance averaged over the altitudes, latitudes, longitudes, L_s , and local times observed by ultraviolet and visible spectrometer (UVIS). The results are shown after applying the same two-dimensional convolution of Δ latitude = 5° in the latitudinal dimension (x axis) and $\Delta z = 3$ km in the altitude dimension (y axis) as the ones in Figure 6 where UVIS retrievals are shown. Panel a shows the GEM vertical distribution of ozone centered at the beginning of northern spring in the L_s range 315° – 45° . Panel b shows the GEM vertical distribution of ozone at the beginning of northern summer in the L_s range 45° – 135° . Panel c shows the GEM vertical distribution of ozone at the beginning of southern spring in the L_s range 135° – 225° . Panel d shows the GEM-Mars vertical distribution of ozone at the beginning of southern summer in the L_s range 225° – 315° . Panels (e–h) are the same UVIS data from Figure 5 shown for comparison.

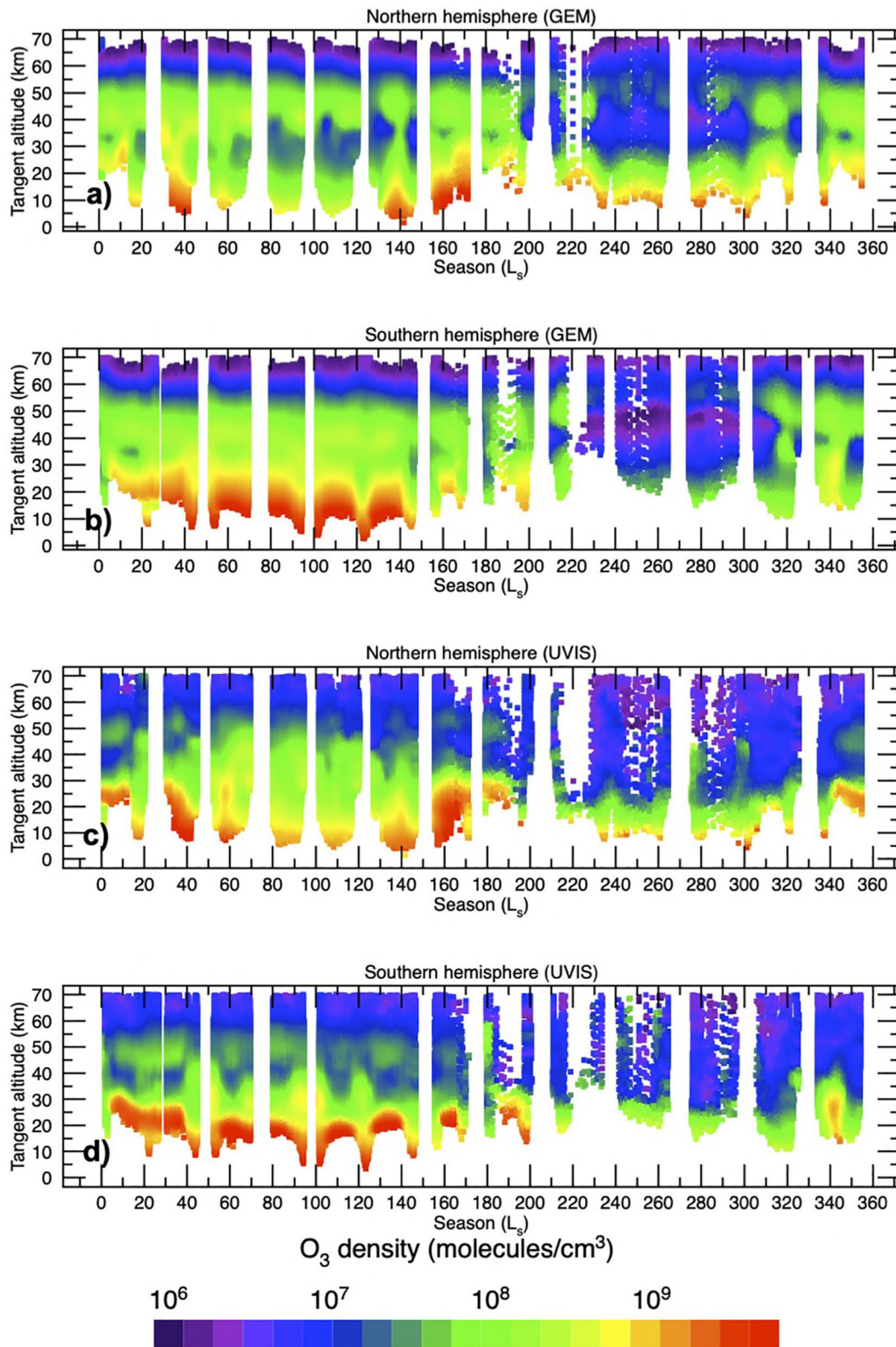


Figure 14.

peaks, and that could be attributed to the effect of the global dust storm within that period of the Martian year during the MY 34 (e.g., Guzewich et al., 2019; Smith, 2019). Dedicated simulations for the global dust storm were presented in Neary et al. (2020), and a study showing the impact the dust storm had on ozone abundances is underway by Daerden et al. The high-altitude peak seen by UVIS at $L_s = 350^\circ$ between the 40 and 50-km altitude is well produced by GEM-Mars, but with ~ 5 times higher O_3 abundances compared to UVIS, again as a result of the low water vapor abundances simulated at high altitude/high latitudes (Aoki et al., 2019; Daerden et al., 2019).

In the southern hemisphere (Figure 14b), the key features in the high-altitude peak of ozone are well depicted in the GEM-Mars results, notably around $L_s = 20^\circ, 65^\circ,$ and 130° . In particular, the peak location in the altitude range 40–50 km throughout southern fall and winter is consistent with the UVIS retrievals. The high-altitude peak in the south polar latitudes is more prominent compared to its counterpart in the north and it persists for over two seasons on Mars, something that is well reproduced in the GEM-Mars simulations. However, the GEM-Mars results again predict higher ozone abundance in the high-altitude peak that are as much as 5 times larger than the retrieved abundances by UVIS. In the southern summer at $\sim L_s = 340^\circ$, an enhancement of ozone at about 30 km is observed in both the UVIS and the GEM-Mars results, but GEM-Mars produced a high-altitude peak between $\sim L_s = 340^\circ$ and 360° that is not found in the UVIS retrievals. As for the northern observations, the differences in the GEM-Mars simulations with the data can here also be attributed to biases in the simulated water vapor abundances, as shown and discussed before (Aoki et al., 2019; Daerden et al., 2019).

6. Discussion and Summary

The stellar occultations by SPICAM (Lebonnois et al., 2006) provided nighttime vertical profiles of ozone between spring equinox and winter solstice. The observations, when combined with theoretical studies (Montmessin & Lefèvre, 2013) to cover polar regions, reported the presence of an elevated layer of ozone between 40 and 60 km in altitude in the southern polar night, repeatedly observed during three Mars years. This layer is predicted to appear essentially during the night when ozone is formed, before being rapidly photolyzed after sunrise (Montmessin & Lefèvre, 2013, 2017). However, retrievals using UVIS solar occultations shown here have detected the strong presence of a high-altitude layer of ozone in the same altitude range (Figures 8a and 8b). UVIS shows a similar pattern in the ozone abundance and peak location in the sunrise and sunset occultations. Indeed, the high-altitude peak in the south polar region persisted throughout the entire southern fall and winter seasons, with a slight decrease in intensity during southern winter, before completely disappearing for the rest of the year and reemerging at $\sim L_s = 330^\circ$ (Figure 4f).

General circulations models (Montmessin & Lefèvre, 2013) attribute the formation of the nocturnal layer to the large-scale transport of oxygen in the Martian atmosphere from midlatitude regions illuminated by solar flux to the polar regions where oxygen atoms recombine at night to form ozone in the high-altitude layer. SPICAM provided observations in the north polar region during northern autumn and winter ($L_s = 180^\circ$ – 360°) but could not identify a pronounced high-altitude layer, a conclusion shared by the GCM model for the north polar latitudes. As a result, Montmessin and Lefèvre (2013) concluded that the aforementioned large-scale transport of oxygen is less efficient in the north, and that the destruction of ozone through reactions with hydrogen radicals is ~ 100 times stronger above the northern winter pole compared to its southern counterpart, ruling out the formation of a secondary layer of ozone in the north polar regions. However, the more complete coverage provided by UVIS indicates that the formation of a high-altitude ozone layer in the north polar regions does occur at the end of northern winter at $L_s = 330^\circ$ (Figures 3f and 6a), lasting until midnorthern spring at $L_s = 45^\circ$ (Figures 3a, 3b, and 6a), but its magnitude and seasonal extent are smaller compared to their counterparts in the south.

Figure 14. Global Environmental Multiscale (GEM)-Mars model simulations of the seasonal distribution of the retrieved vertical O_3 abundance (molecules/cm³) averaged over the altitudes, latitudes, longitudes, L_s , and local times observed by ultraviolet and visible spectrometer (UVIS) in the northern (panel a) and southern (panel b) hemispheres. The results are shown after applying similar two-dimensional convolution of $\Delta L_s = 5^\circ$ in the local time dimension (x axis) and $\Delta z = 3$ km in the altitude dimension (y axis) as the ones in Figure 12 where UVIS retrievals are shown. Panels (c and d) are the same UVIS data from Figure 12 shown for comparison.

In summary, the UVIS spectrometer onboard TGO provided $\sim 4,100$ solar occultation profiles of the atmosphere of Mars covering a full Mars year between MY 34 at $L_s = 163^\circ$ on April 21, 2018, and MY 35 on March 9, 2020. UVIS retrievals provide the most complete vertical O_3 mapping ever produced, describing the seasonal, spatial and local time distribution of ozone in detail.

UVIS retrievals reveal the presence of a high-altitude peak of ozone between 40 and 60 km in altitude over the north polar latitudes for at least 45% of the Martian year, particularly during midnorthern spring, late northern summer-early southern spring, and late southern summer. UVIS also detected the presence of a second high-altitude peak in the south polar latitudes, lasting for at least 60% of the year including southern autumn and winter. The evolution of the high-altitude O_3 peak on the hemispheric scale shows that it is more prominent in the south and is mostly confined to latitudes poleward of $60^\circ S$. This high-altitude peak shows similarities in location during the first half of southern fall and the second half of southern winter with its counterpart over the north polar latitudes. Local time distribution of the retrieved vertical profiles of O_3 show that the high-altitude peaks in the north and south polar regions show a lack of variability in magnitude and location with respect to the variations in the local time. In contrast, no high-altitude peak of ozone was observed at equatorial latitudes at any time throughout the Martian year.

Given how complicated it is to model the vertical distribution of ozone, the GEM-Mars model results are able to very well reproduce the general behavior of the high-altitude peak of ozone when compared to the UVIS O_3 retrievals. In particular, the GEM-Mars predicts the presence of high-altitude peaks of ozone at polar latitudes around the beginning of northern spring and autumn and at the same altitudes observed by UVIS retrievals. In addition, the GEM-Mars model results accurately predict that the high-altitude peak in the south polar latitudes is more prominent compared to its counterpart in the north and that it persists for more than two seasons on Mars. Differences include higher GEM-Mars ozone abundance in the high-altitude peaks, reaching a factor of 5 in some occasions, leading to a larger vertical extent in the atmosphere than what is observed by UVIS. GEM-Mars also predicts the presence of a high-altitude peak of ozone around northern summer between latitudes 30° and $60^\circ N$ that is not observed as an independent layer by UVIS. The same ability to predict the high-altitude peaks in ozone abundance is evidenced in the modeling results in the companion paper to this study (Patel et al., 2021), where the GCM outputs from the Open University model simulation show the same pattern of ozone enhancements.

All the differences between GEM-Mars and the observations can be attributed to underestimate or overestimate of water vapor abundances in the model, which were already presented and discussed in previous works (Aoki et al., 2019; Daerden et al., 2019). The strong anticorrelation between ozone and water vapor caused by the action of HO_x chemistry resulting from water vapor photolysis, can then readily explain the bias in ozone. Improvements in the simulation of the water cycle envisaged in the GEM-Mars model, which includes cloud formation, microphysics, radiative feedbacks, dust scavenging, etc., may improve the simulation of water vapor profiles in the future and improve the comparisons with the ozone profiles presented here.

Data Availability Statement

The TGO data are publicly available through the European Space Agency's Planetary Science Archive (archives.esac.esa.int/psa/) with additional access to NOMAD data through the PI institute (nomad.aeronomie.be). The derived ozone retrieval data set and the modeling and assimilation data that support the plots within this paper are available through the following data citation reference: Patel (2021). The GEM model results presented in this manuscript are available at the following data citation reference: Daerden (2021). Alain Khayat would like to thank Monique Myriam Nasrallah, Salma, and Joseph Khayat for their patience and support throughout the preparation of this work.

Acknowledgments

This work was supported by the NASA's Mars Program Office under WBS 604796, "Participation in the TGO/NOMAD Investigation of Trace Gases on Mars." The material was based upon the work supported by the NASA under award No. 80GSFC21M0002. The NOMAD experiment was led by the Royal Belgian Institute for Space Aeronomy (IASB-BIRA), assisted by Co-PI teams from Spain (IAA-CSIC), Italy (INAF-IAPS), and the United Kingdom (Open University). This project acknowledges funding by the Belgian Science Policy Office (BELSPO), with the financial and contractual coordination by the ESA Prodex Office (PEA 4000103401, 4000121493), by the Spanish Ministry of Science and Innovation (MCIU) and by the European funds under grants PGC2018-101836-B-I00 and ESP2017-87143-R (MINECO/FEDER), as well as by the UK Space Agency through Grants ST/V002295/1, ST/P001262/1, ST/S00145X/1, and ST/V005332/1 and Italian Space Agency through Grant 2018-2-HH.0. This work was supported by the Belgian Fonds de la Recherche Scientifique—FNRS under Grant No. 30442502 (ET_HOME). This project has received funding from the European Union's Horizon 2020 research and innovation programme under Grant Agreement No. 101004052 (RoadMap project). The IAA/CSIC team acknowledges financial support from the State Agency for Research of the Spanish MCIU through the "Center of Excellence Severo Ochoa" award for the Instituto de Astrofísica de Andalucía (SEV-2017-0709). US investigators were supported by the National Aeronautics and Space Administration. Canadian investigators were supported by the Canadian Space Agency.

References

Aoki, S., Vandaele, A. C., Daerden, F., Villanueva, G. L., Liuzzi, G., Thomas, I. R., et al. (2019). Water vapor vertical profiles on Mars in dust storms observed by TGO/NOMAD. *Journal of Geophysical Research: Planets*, *124*, 3482–3497. <https://doi.org/10.1029/2019JE006109>

Auvinen, H., Oikarinen, L., & Kyrölä, E. (2002). Inversion algorithms for recovering minor species densities from limb scatter measurements at UV-visible wavelengths. *Journal of Geophysical Research*, *107*(D13), 4172. <https://doi.org/10.1029/2001JD000407>

Barth, C. A., & Hord, C. W. (1971). Mariner ultraviolet spectrometer: Topography and polar cap. *Science*, *173*(3993), 197–201. <https://doi.org/10.1126/science.173.3993.197>

Barth, C. A., Hord, C. W., Stewart, A. I., & Lane, A. L. (1972). Mariner 9 ultraviolet spectrometer experiment: Initial results. *Science*, *175*(4019), 309–312. <https://doi.org/10.1126/science.175.4019.309>

Barth, C. A., Hord, C. W., Stewart, A. I., Lane, A. L., Dick, M. L., & Anderson, G. P. (1973). Mariner 9 ultraviolet spectrometer experiment: Seasonal variation of ozone on Mars. *Science*, *179*(4075), 795–796. <https://doi.org/10.1126/science.179.4075.795>

Blamont, J. E., & Chassefière, E. (1993). First detection of ozone in the middle atmosphere of Mars from solar occultation measurements. *Icarus*, *104*(2), 324–336. <https://doi.org/10.1006/icar.1993.1104>

Clancy, R. T., & Nair, H. (1996). Annual (perihelion-aphelion) cycles in the photochemical behavior of the global Mars atmosphere. *Journal of Geophysical Research*, *101*(E5), 12785–12790. <https://doi.org/10.1029/96JE00836>

Clancy, R. T., Wolff, M. J., James, P. B., Smith, E., Billawala, Y. N., Lee, S. W., & Callan, M. (1996). Mars ozone measurements near the 1995 aphelion: Hubble Space Telescope ultraviolet spectroscopy with the faint object spectrograph. *Journal of Geophysical Research*, *101*(E5), 12777–12783. <https://doi.org/10.1029/96JE00835>

Clancy, R. T., Wolff, M. J., Lefèvre, F., Cantor, B. A., Malin, M. C., & Smith, M. D. (2016). Daily global mapping of Mars ozone column abundances with MARCI UV band imaging. *Icarus*, *266*, 112–133. <https://doi.org/10.1016/j.icarus.2015.11.016>

Daerden, F. (2021). *GEM-Mars GCM simulations of O₃ for NOMAD-UVIS profile geometries published in Khayat et al. (2021)*. Royal Belgian Institute for Space Aeronomy (BIRA-IASB). <https://doi.org/10.18758/71021066>

Daerden, F., Neary, L., Viscardi, S., García Muñoz, A., Clancy, R. T., Smith, M. D., et al. (2019). Mars atmospheric chemistry simulations with the GEM-Mars general circulation model. *Icarus*, *326*, 197–224. <https://doi.org/10.1016/j.icarus.2019.02.030>

Espenak, F., Mumma, M. J., Kostiuk, T., & Zipoy, D. (1991). Ground-based infrared measurements of the global distribution of ozone in the atmosphere of Mars. *Icarus*, *92*, 252–262. [https://doi.org/10.1016/0019-1035\(91\)90049-y](https://doi.org/10.1016/0019-1035(91)90049-y)

Fast, K., Kostiuk, T., Espenak, F., Annen, J., Buhl, D., Hewagama, T., et al. (2006). Ozone abundance on Mars from infrared heterodyne spectra. I. Acquisition, retrieval, and anticorrelation with water vapor. *Icarus*, *181*, 419–431. <https://doi.org/10.1016/j.icarus.2005.12.001>

Gröller, H., Montmessin, F., Yelle, R. V., Lefèvre, F., Forget, F., Schneider, N. M., et al. (2018). MAVEN/IUVS stellar occultation measurements of Mars atmospheric structure and composition. *Journal of Geophysical Research: Planets*, *123*, 1449–1483. <https://doi.org/10.1029/2017JE005466>

Guzewich, S. D., Lemmon, M., Smith, C. L., Martínez, G., de Vicente-Retortillo, Á., Newman, C. E., et al. (2019). Mars science laboratory observations of the 2018/Mars year 34 global dust storm. *Geophysical Research Letters*, *46*, 71–79. <https://doi.org/10.1029/2018GL080839>

Ityakov, D., Linnartz, H., & Ubachs, W. (2008). Deep-UV absorption and Rayleigh scattering of carbon dioxide. *Chemical Physics Letters*, *462*, 31–34. <https://doi.org/10.1016/j.cplett.2008.07.049>

Lebonnois, S., Quémerais, E., Montmessin, F., Lefèvre, F., Perrier, S., Bertaux, J.-L., & Forget, F. (2006). Vertical distribution of ozone on Mars as measured by SPICAM/Mars Express using stellar occultations. *Journal of Geophysical Research*, *111*, E09S05. <https://doi.org/10.1029/2005JE002643>

Lefèvre, F., Bertaux, J.-L., Perrier, S., Lebonnois, S., Korabiev, O., Fedorova, A., et al. (2007). The Martian ozone layer as seen by SPICAM/Mars-express. *LPI Contributions*.

Lefèvre, F., Lebonnois, S., Montmessin, F., & Forget, F. (2004). Three-dimensional modeling of ozone on Mars. *Journal of Geophysical Research*, *109*, E07004. <https://doi.org/10.1029/2004JE002268>

Malin, M. C., Calvin, W., Clancy, R. T., Haberle, R. M., James, P. B., Lee, S. W., et al. (2001). The Mars Color Imager (MARCI) on the Mars climate orbiter. *Journal of Geophysical Research*, *106*(E8), 17651–17672. <https://doi.org/10.1029/1999JE001145>

Malin, M. C., Calvin, W. M., Cantor, B. A., Clancy, R. T., Haberle, R. M., James, P. B., et al. (2008). Climate, weather and north polar observations from the Mars Reconnaissance Orbiter Mars Color Imager. *Icarus*, *194*, 501–512. <https://doi.org/10.1016/j.icarus.2007.10.016>

Markwardt, C. B. (2009). Non-linear least-squares fitting in IDL with MPFIT. In D. A. Bohlender, D. Durand, & P. Dowler (Eds.), *Astronomical Data Analysis Software and Systems XIV* (Vol. XVIII, pp. 251).

Montmessin, F., Korabiev, O., Lefèvre, F., Bertaux, J.-L., Fedorova, A., Trokhimovskiy, A., et al. (2017). SPICAM on Mars Express: A 10 year in-depth survey of the Martian atmosphere. *Icarus*, *297*, 195–216. <https://doi.org/10.1016/j.icarus.2017.06.022>

Montmessin, F., & Lefèvre, F. (2013). Transport-driven formation of a polar ozone layer on Mars. *Nature Geoscience*, *6*, 930–933. <https://doi.org/10.1038/ngeo1957>

Navarro, T., Madeleine, J.-B., Forget, F., Spiga, A., Millour, E., Montmessin, F., & Määttä, A. (2014). Global climate modeling of the Martian water cycle with improved microphysics and radiatively active water ice clouds. *Journal of Geophysical Research: Planets*, *119*, 1479–1495. <https://doi.org/10.1002/2013JE004550>

Neary, L., & Daerden, F. (2018). The GEM-Mars general circulation model for Mars: Description and evaluation. *Icarus*, *300*, 458–476. <https://doi.org/10.1016/j.icarus.2017.09.028>

Neary, L., Daerden, F., Aoki, S., Whiteway, J., Clancy, R. T., Smith, A. C., et al. (2020). Explanation for the increase in high-altitude water on Mars observed by NOMAD during the 2018 global dust storm. *Geophysical Research Letters*, *47*, e2019GL084354. <https://doi.org/10.1029/2019GL084354>

Novak, R. E., Mumma, M. J., DiSanti, M. A., & Dello Russo, N. (2002). Mapping of ozone and water in the atmosphere of Mars near the 1997 aphelion. *Icarus*, *158*, 14–23. <https://doi.org/10.1006/icar.2002.6863>

Noxon, J. F., Traub, W. A., Carleton, N. P., & Connes, P. (1976). Detection of O₂ dayglow emission from Mars and the Martian ozone abundance. *The Astrophysical Journal*, *207*, 1025–1035. <https://doi.org/10.1086/154572>

Olsen, K. S., Lefèvre, F., Montmessin, F., Trokhimovskiy, A., Baggio, L., & Fedorova, A. (2020). First detection of ozone in the mid-infrared at Mars: Implications for methane detection. *Astronomy and Astrophysics*, *639*, A141. <https://doi.org/10.1051/0004-6361/202038125>

Patel, M., Antoine, P., Mason, J., Leese, M., Hathi, B., Stevens, A., et al. (2017). NOMAD spectrometer on the ExoMars Trace Gas Orbiter mission: Part 2—Design, manufacturing, and testing of the ultraviolet and visible channel. *Applied Optics*, *56*, 2771–2782. <https://doi.org/10.1364/ao.56.002771>

Patel, M. R. (2021). *Dataset in support of paper "ExoMars TGO/NOMAD-UVIS profiles of ozone in Mars years 34-35: Part 1—Vertical distribution and comparison to water"* [Data Set]. Open Research Data Online (ORDO) Repository. <https://doi.org/10.21954/ou.rd.13580336>

- Patel, M. R., Sellers, G., Mason, J. P., Holmes, J. A., Brown, M. A. J., Lewis, S. R., et al. (2021). ExoMars TGO/NOMAD-UVIS vertical profiles of ozone: Part 1 – Seasonal variation and comparison to water. *Journal of Geophysical Research: Planets*, *126*, e2021JE006837. <https://doi.org/10.1029/2021JE006837>
- Perrier, S., Bertaux, J. L., Lefèvre, F., Lebonnois, S., Korabiev, O., Fedorova, A., & Montmessin, F. (2006). Global distribution of total ozone on Mars from SPICAM/MEX UV measurements. *Journal of Geophysical Research*, *111*, E09S06. <https://doi.org/10.1029/2006JE002681>
- Picciali, A., Vandaele, A. C., Trompet, L., Neary, L., Viscardy, S., Erwin, J. T., et al. (2021). Impact of gradients at the Martian terminator on the retrieval of ozone from SPICAM/MEX. *Icarus*, *353*, 113598. <https://doi.org/10.1016/j.icarus.2019.113598>
- Quémerais, E., Bertaux, J.-L., Korabiev, O., Dimarellis, E., Cot, C., Sandel, B. R., & Fussen, D. (2006). Stellar occultations observed by SPICAM on Mars Express. *Journal of Geophysical Research*, *111*, E09S04. <https://doi.org/10.1029/2005JE002604>
- Rodgers, C. D. (2000). *Inverse methods for atmospheric sounding* (p. 238). World Scientific.
- Shaposhnikov, D. S., Rodin, A. V., Medvedev, A. S., Fedorova, A. A., Kuroda, T., & Hartogh, P. (2018). Modeling the hydrological cycle in the atmosphere of Mars: Influence of a bimodal size distribution of aerosol nucleation particles. *Journal of Geophysical Research: Planets*, *123*, 508–526. <https://doi.org/10.1002/2017JE005384>
- Smith, M. D. (2019). THEMIS observations of the 2018 Mars global dust storm. *Journal of Geophysical Research: Planets*, *124*, 2929–2944. <https://doi.org/10.1029/2019JE006107>
- Smith, M. D., Daerden, F., Neary, L., & Khayat, A. (2018). The climatology of carbon monoxide and water vapor on Mars as observed by CRISM and modeled by the GEM-Mars general circulation model. *Icarus*, *301*, 117–131. <https://doi.org/10.1016/j.icarus.2017.09.027>
- Vandaele, A., Willame, Y., Depiesse, C., Thomas, I., Robert, S., Bolsée, D., et al. (2015). Optical and radiometric models of the NOMAD instrument part I: The UVIS channel. *Optics Express*, *23*, 30028–30042. <https://doi.org/10.1364/oe.23.030028>
- Vandaele, A. C., Lopez-Moreno, J., Patel, M. R., Patel, M. R., Bellucci, G., Daerden, F., et al. (2018). NOMAD, an integrated suite of three spectrometers for the ExoMars Trace Gas Mission: Technical description, science objectives and expected performance. *Space Science Reviews*, *214*, 80. <https://doi.org/10.1007/s11214-018-0517-2>
- Willame, Y., Vandaele, A. C., Depiesse, C., Lefevre, F., Letocart, V., Gillotay, D., & Montmessin, F. (2017). Retrieving cloud, dust and ozone abundances in the Martian atmosphere using SPICAM/UV nadir spectra. *Planetary and Space Science*, *142*, 9–25. <https://doi.org/10.1016/j.pss.2017.04.011>